Pulsed melt flux controls the rheological evolution and widening of a melt-present high strain zone

H. Ghataka, N. R. Daczkoa, S. Piazolob, and T. Raimondoc, d

^aSchool of Natural Sciences, Macquarie University, Australia; ^bSchool of Earth and Environment, University of Leeds, Leeds, United Kingdom; ^cUniSA STEM, University of South Australia, Australia; ^dSchool of Physics, Chemistry and Earth Sciences, Adelaide University, Australia

ORCID

 H. Ghatak
 https://orcid.org/0000-0001-8998-033X

 N. R. Daczko
 https://orcid.org/0000-0002-3737-3818

 S. Piazolo
 https://orcid.org/0000-0001-7723-8170

 T. Raimondo
 https://orcid.org/0000-0001-9115-9196

ARTICLE HISTORY

Received 21 September 2025 Accepted 19 November 2025

CONTACT Nathan Daczko **email** <u>nathan.daczko@mq.edu.au</u> **mail** School of Natural Sciences, Macguarie University, NSW 2109, Australia

Abstract

High-strain deformation zones accommodate much of the strain during orogenic shortening through localised weakening. However, once a weakened zone develops, it should inhibit the formation of wide high-strain zones (hundreds of meters to kilometres across), making their origin contentious. We address this problem by studying the 100-300 m wide, garnet-biotite-rich Cattle Water Pass shear zone in the intracontinental Alice Springs Orogen, central Australia. Microstructural features, including cuspate grain shapes, low dihedral angles, "string of beads" textures, and thin elongate grains of plagioclase and quartz, indicate deformation in the presence of melt. Quantitative crystallographic orientation data show three-dimensional plagioclase connectivity and limited quartz and ilmenite deformation in highly modified samples, consistent with syn-deformational melt crystallisation. Wholerock geochemistry and major-, trace-, and REE-element variations demonstrate that deformation occurred in an open system, buffered by fluxing melt. Cathodoluminescence textures and local chemical variations in feldspar and biotite further support melt-rock interaction during deformation. Variably hydrated domains across the shear zone suggest spatially heterogeneous melt flux. The magnitude of rheological weakening caused by syn-deformational melt fluxing precludes formation of the entire high-strain zone in a single event; instead, the melt-rock reacted domains must reflect multiple episodes of melt ingress, reaction and egress. The absence of cross-cutting relationships indicates that each event preserved earlier domains, with new strain localising along weaker interfaces or in adjacent, less-strained regions. We propose a model in which successive melt pulses progressively widen the shear zone as the melt conduit network expands.

KEYWORDS

melt-rock interaction; melt-present deformation; pulsed melt flow; shear zone widening; central Australia; Alice Springs Orogeny

KEY POINTS

- 1. Microstructures indicate syn-deformational melt presence and reaction-driven transformation.
- 2. Episodic melt pulses drive open-system melt-rock interaction.
- 3. Rheological weakening through melt-assisted deformation and reaction.
- 4. Progressive shear zone widening through cyclical melt reactivation.

Editorial handling: Chris Fergusson

Introduction

Faults and shear zones are crustal-scale weak zones that accommodate stress during orogenesis. Broadly, faults reflect brittle deformation, whereas shear zones record strain localisation in the ductile regime (Fossen & Cavalcante, 2017; Sibson, 1977). Shear zones can exhibit a range of dynamic behaviours through their evolution, including widening, narrowing, maintaining a near-constant width, or migrating spatially ("jumping") into adjacent regions. These variations reflect the interplay between strain rate, rheological contrast, fluid availability, and thermal conditions, which together control whether deformation becomes increasingly localised or distributed over time (Holyoke & Tullis, 2006). Shear zone widening can be promoted by strain hardening processes such as dislocation accumulation, dehydration, and the growth of stronger minerals (Hull, 1988; Means, 1984, 1995; Oliot et al., 2014). For example, the Himalayan Main Central Thrust is a several-hundred-metre-thick highstrain zone that accommodates 185–245 km of shortening (Martin et al., 2005; Schelling & Arita, 1991).

Over the last decades, it has become clear that brittle and ductile deformation modes are closely linked across crustal levels and may even occur simultaneously (Fusseis *et al.*, 2006; Simpson, 1985). High-strain zones formed in this way are commonly reactivated, localising strain during subsequent tectonic events (D'Lemos *et al.*, 1997; Piazolo *et al.*, 2020). However, rheological hardening can limit reactivation potential. Hardening mechanisms, often the reverse of weakening processes (Gardner *et al.*, 2020), include grain coarsening (Bürgmann & Dresen, 2008; Rybacki & Dresen, 2004), reaction hardening (Hobbs *et al.*, 2010; White & Knipe, 1978), deformation mechanism switches (Smith *et al.*, 2015), modal reduction of deformable phases (Cyprych *et al.*, 2016; Ji *et al.*, 2001), and loss of fluids or melts (Finch *et al.*, 2016; Renner *et al.*, 2000).

Reactivation is broadly defined as the accommodation of geologically distinct deformation events along pre-existing structures, including faults, shear zones, rheological boundaries, and magma ascent pathways (Holdsworth *et al.*, 1997). Two end-member types can be distinguished: (1) reactivation of structures under new tectonic regimes or P–T conditions, such as extensional faults inverted during compression (Sibson, 1995), and (2) repeated activation of high-strain zones during a single orogenic cycle, separated by quiescent intervals. Earthquake cycles exemplify the latter, where episodic slip is modulated by transient fluid flow (Byerlee, 1993; Mugnier *et al.*, 2004; Sibson, 1990; Wallace, 1984). Because many of these processes depend on fluid availability, fluids are a critical control on both the initiation and cessation of reactivation (Zhang *et al.*, 2011).

Fluids and melts strongly influence shear zone rheology. Free fluids reduce rock strength and localise strain (Wintsch *et al.*, 1995; Yardley, 2009). Transient fluid pulses drive fracturing, veining, and mineral replacements, promoting grain-size reduction and reaction softening through transformation of stronger minerals into weaker minerals, such as phyllosilicates (Brodie & Rutter, 1987; Holdsworth *et al.*, 2001; Stewart *et al.*, 2000; Wallis *et al.*, 2013, 2015; Wibberley, 1999). Similarly, melt-present deformation produces intrinsically weak high-strain zones (Piazolo *et al.*, 2020; Rutter & Neumann, 1995; Van der Molen & Paterson, 1979), with >7 vol.% melt reducing rock strength by at least an order of magnitude (Lee *et al.*, 2018; Rosenberg & Handy, 2005). Melt flux facilitates both strain weakening and strengthening, depending on its connectivity, chemistry, and timing (Brown & Solar, 1998; Handy *et al.*, 2001; Rosenberg & Handy, 2005).

Pulsed melt infiltration provides an effective mechanism for episodic weakening and shear zone reactivation. Each melt pulse lowers viscosity, introduces hydrous phases, and enhances grain-boundary processes such as dissolution—precipitation and diffusion creep (Daczko *et al.*, 2016; Hacker, 1997). Subsequent melt extraction or crystallisation may trigger strengthening through grain coarsening, loss of the fluid phase, or growth of stronger mineral frameworks (Rosenberg & Handy, 2005). This cyclic weakening—strengthening behaviour governs the episodic activity of deep crustal shear zones (Piazolo *et al.*, 2020). However, under suprasolidus conditions, persistent melt connectivity limits re-strengthening, favouring sustained weakening and ductile flow. Repeated melt pulses may therefore drive progressive shear zone widening, as strain migrates into previously stronger wall rocks through melt-assisted deformation and melt–rock reactions (Chatterjee *et al.*, 2024; Lee *et al.*, 2020; Weinberg & Hasalová, 2015; Yakymchuk & Brown, 2014).

The intracontinental Alice Springs Orogen of central Australia provides an ideal setting to investigate these processes. Shear zones in this orogen are wide (>2 km; Bendall, 2000; Norman, 1991) and record multiple reactivation events associated with Ordovician—Carboniferous tectonism (Piazolo *et al.*, 2020; Raimondo *et al.*, 2014). Previous studies have documented evidence for hydration, metasomatism, and melt infiltration, suggesting that open-system behaviour facilitated

episodic weakening and contributed to the long-lived Alice Springs Orogeny (450–300 Ma; Asimus et al., 2023; Ghatak et al., 2022, 2025; Silva et al., 2022, 2023; Varga et al., 2022).

In this study, we examine the Cattle Water Pass shear zone with the aim of identifying microstructural and microchemical evidence for reactivation via pulsed melt infiltration. We focus on how syn-deformational melt presence controlled the development and rheological evolution of biotiterich rocks, and how these processes contributed to shear zone widening. We focus on the modification of felsic granulites as these provide a well-characterised, high-grade protolith whose relatively anhydrous mineral assemblages can be directly contrasted to the hydration and weakening that we document during shear zone development. Understanding the resulting biotite modal gradient is significant, as it records the progressive transformation of strong, dry granulites into weaker, hydrous assemblages, offering key insights into the mechanisms that localise deformation in the middle to lower crust. Unlike traditional subsolidus shear zones that record overprinting fabrics associated with changing stress regimes (Passchier & Trouw, 2005), our study targets deformation under a consistent stress field, along persistent structural planes. This framework highlights the role of internal reworking and progressive strain localisation under suprasolidus conditions (Lee *et al.*, 2020; Rosenberg & Handy, 2005).

Geological background

The study area lies within the central Australian Arunta region, a 200,000 km² inlier of polydeformed Proterozoic rocks (Figure 1a). The last major tectonism and exhumation occurred during the upper Paleozoic Alice Springs Orogeny (450–300 Ma; Hand & Sandiford, 1999; Raimondo *et al.*, 2014). From west to east, the Alice Springs Orogeny encompasses the mid-crustal Reynolds–Anmatjira Ranges (immediately northwest of the map in Figure 1a), the mid- to deep-crustal Strangways Metamorphic Complex, and the deep-crustal Harts Range Group at the southeastern extremity of the Arunta (Figure 1). The Alice Springs Orogeny was intraplate in nature, involving north-south contraction and up to ~100 km of horizontal shortening in the eastern Arunta (Collins & Teyssier, 1989; Silva *et al.*, 2018; Teyssier, 1985). This deformation exhumed mid- to deep-crustal rocks and produced an anastomosing network of shear zones across the region (Cartwright *et al.*, 1999; Raimondo *et al.*, 2011). Geochronological and sedimentological data indicate that the Alice Springs Orogeny was episodic, comprising several pulses of deformation over a ~150 Myr interval, possibly controlled by melt availability in the lower crust (Buick *et al.*, 2008; Haines *et al.*, 2001; Piazolo *et al.*, 2020; Raimondo *et al.*, 2014).

The present study focuses on the Strangways Range within the Strangways Metamorphic Complex, a ~125 km-wide belt that formed during the *ca* 1730 Ma Strangways Orogeny (Maidment *et al.*, 2005). Kilometre-scale, steeply dipping Proterozoic shear zones within the complex were reactivated during the Alice Springs Orogeny, forming amphibolite- to greenschist-facies schist belts dominated by south-directed thrusting (Bendall, 2000; Collins & Teyssier, 1989). Among these is the Cattle Water Pass shear zone (CWPSZ), a 100–300 m wide, steeply east- to south-dipping reverse shear zone in the eastern Strangways Range. It is defined by sillimanite—garnet—muscovite—biotite schist formed during melt-present deformation (Figure 1b; Ghatak *et al.*, 2025). Shear zones of Alice Springs Orogeny age (450–300 Ma) in both the Strangways and nearby Harts Range are spatially associated with syn- to post-tectonic pegmatite dykes (Buick *et al.*, 2008), though the origin of these pegmatites remains debated.

Methods and analytical techniques

Petrography

Polished thin sections (30 µm thick) were made from blocks cut perpendicular to the foliation and parallel to lineation. These sections of the samples were used for petrographical analysis. Mineral identification and microstructural investigation of the samples used optical microscopy under plane and crossed polarised light (Macquarie University, Sydney, Australia) and the virtual petrographic microscope (Tetley & Daczko, 2014). Back-scatter electron (BSE) imaging was performed on a Hitachi Desktop Scanning Electron microscope (SEM; OptoFab node of the Australian National Fabrication Facility, Macquarie University). The operating conditions of the SEM were low vacuum and 15 kV accelerating voltage. Whitney and Evans (2010) are followed for mineral abbreviations.

X-ray mapping

Micro X-ray fluorescence (μ XRF) mapping was carried out using a Bruker M4 Tornado equipped with an Rh x-ray tube and dual Bruker x-flash EDS detectors. The analysis was carried out at 50kV, and 200 μ A and maps were collected with a 25 μ m spot size and 60 μ m step. Data were processed using the Bruker M4 Esprit software package.

Mineral major element composition: electron microprobe

Compositional analyses of silicates were acquired using a JEOL JXA 8530F Plus field emission electron microprobe (EPMA) at the central science laboratory, University of Tasmania. The instrument is equipped with a field emission source, and an accelerating voltage of 15kV, a beam current of 15nA and a beam size of 10µm were used for analysing the samples. The instrument has five wavelength dispersive spectrometers and is operated using the Probe Software Inc. "Probe For EPMA" software package. The data set is presented in the Supplemental data.

Mineral trace element composition: laser ablation inductively coupled plasma mass spectrometry

The concentration of rare earth elements in biotite, plagioclase and garnet was determined in thin section with a laser ablation inductively coupled plasma mass spectrometer (LA-ICPMS) at Macquarie GeoAnalytical (MQGA), Sydney, Australia. The instrument used for the analysis was an Agilent 7700cx quadrupole ICPMS attached to a Photon Machines Excite 193 nm excimer laser ablation system fitted with HelEx two-volume sample cell. Analyses were obtained using a spot size of 85 µm with a pulse rate of 10Hz and laser energy ~5 J cm-2. Silicon (measured by electron microprobe) was used as an internal standard for all minerals, and NIST 610 and 612, and basalt from the Columbia River (BCR-2) were used as external standards. The raw data was processed using the GLITTERTM software package (Version 4.4), which enhanced the data quality (Griffin *et al.*, 2008; http://www.glitter-gemoc.com/). The data set is presented in the Supplemental data.

Quantitative crystallographic orientation analysis: electron backscatter diffraction

Microstructural/crystallographic characterisation of samples was performed using an FEI Quanta 650 FEG-scanning electron microscope (SEM) with AZtec software and an Oxford/HKL Nordlys EBSD system at the Electron Optics Facility, University of Leeds, UK. Electron back scatter diffraction (EBSD) mapping was performed on an ultra-polished thin section (additional 8 minutes polishing with colloidal silica-water solution) covering large areas of the sample. The sample was coated with \sim 3 nm of carbon. Working conditions were: 20 kV accelerating voltage, \sim 12 mm working distance, 70° specimen tilt and step size 6 µm.

Data were processed using HKL Channel5 v5.11, with noise reduction performed on the raw data following the procedure of Bestmann and Prior (2003). The data has been used to construct phase maps, orientation maps and equal area pole figures plotted in the lower hemisphere. One point per grain eliminates the possibility of large grains distorting the interpretation by causing single-crystal maxima. However, occasionally where no large crystal dominates, all the points were plotted on the pole figures. Adjoining grains have also been plotted on pole figures to be able to assess their relative crystal orientations. To show internal orientation changes in grains, misorientation maps which are colour coded according to the difference in orientation relative to a reference point are shown. These maps are supported by misorientation profiles across grains showing the change in crystallographic orientation with respect to the orientation of the profile starting point.

Field relationships and petrography

Field relationships and sample selection

In the eastern Strangways Range, a prominent 100–300 m wide, steeply east- to south-dipping shear zone cuts across Proterozoic felsic granulites of the Strangways Metamorphic Complex (Ghatak *et al.*, 2022). This shear zone is strongly anastomosing and characterised by sillimanite–garnet–biotite

schist that encloses pods of variably modified granulite. Near the study area, foliation dips $80-85^{\circ}$ towards $190-200^{\circ}$. Stretching lineations pitch moderately $(60-70^{\circ})$ toward the southeast. Relict lenses of felsic granulite are locally preserved, while higher strain domains show progressive development of biotite- and muscovite-rich layers (e.g. Figure 2). In places, these micaceous rocks display mylonitic fabrics, including asymmetric strain shadows (σ -type) and S–C fabrics, indicating a top-to-the-west (reverse) shear sense. However, most mica-rich outcrops lack clear shear-sense indicators. Mafic granulite protoliths of the Strangways Metamorphic Complex are also reworked locally into amphibole- \pm garnet-bearing assemblages.

Felsic granulites were distinguished from mafic varieties in the field by their lighter colour, banding of quartzofeldspathic and sillimanite—biotite-rich layers, absence of pyroxene and amphibole, and a locally banded rather than massive appearance. This study focuses on modification of felsic granulites along the shear zone margin. Narrow chlorite—quartz—epidote veins with alteration halos record later, lower-temperature overprinting.

Our aim was to investigate the mechanisms by which thick, biotite-dominated shear zones develop in granulite terranes. For this purpose, we examined felsic granulites that preserve a visible, gradual increase in modal biotite content towards the shear zone. This transformation is marked by the appearance of millimetre- to centimetre-scale biotite—garnet bands (± lenses) that increase in frequency with strain, where we qualitatively estimate strain based on (i) field assessment of foliation intensity, (ii) proportions of relict granulite minerals, and (iii) evaluation of hydration via new hydrous mineral formation. These bands are mostly parallel to the regional foliation, defined by biotite. Towards the shear zone core, felsic granulites evolve into anastomosing micaceous layers, culminating in thick biotite—garnet zones lacking any remnant granulite, indicating hydration of the protolith (Ghatak *et al.*, 2022, 2025).

Our study focuses on a small outcrop of deformed felsic gneiss at the shear zone margin, considered representative of the broader zone. Three samples with variable biotite contents were collected from this single outcrop, each within one metre of the others. None show evidence of low-grade retrogression. Previous studies have demonstrated that such high-strain zones are widespread in the region due to fluid- and melt-induced metasomatic modification (Asimus *et al.*, 2023; Piazolo *et al.*, 2020; Raimondo *et al.*, 2014; Silva *et al.*, 2022, 2023). To avoid protolith heterogeneity, samples were collected from areas where felsic granulite is homogeneous at the 10–100 m scale outside the shear zone, and where relict granulite lenses occur within it (23°11'32.76"S, 134°35'52.57"E).

We classify the three samples based on modal biotite content. The low-biotite sample (low mode or LM; ~10%) consists of coarse quartz (1–4 mm), finer plagioclase, and minor biotite (Figure 2a, d). The medium-biotite sample (medium mode or MM; ~37%) shows field-scale anastomosing bands (Figure 2b, e). The high-biotite sample (high mode or HM; ~57%) is strongly banded, comprising alternating felsic leucosome and biotite—garnet-rich domains (Figure 2c, f). Garnet grains are generally idiomorphic and <1 cm across, although some reach up to 3 cm. Unlike LM and MM, the HM sample is markedly heterogeneous in its biotite-to-garnet ratio.

Because modal increases in biotite and garnet likely reflect modification of the protolith, sampling strategy emphasised: (i) field assessment of strain-related fabric development, guided by orientation and intensity relative to shear zone margins; (ii) petrographic evaluation of relict granulite minerals; and (iii) assessment of hydration degree based on the abundance of new hydrous minerals (Figure 2d, f).

Petrography and microstructure

Low biotite mode (LM) sample

The LM sample comprises quartz (42%), plagioclase (43%), biotite (10%), minor sillimanite (\sim 2%), and magnetite (\sim 3%; Figure 3). A weak foliation is defined by fine- to medium-grained biotite (0.2–3 mm; Figure 3b). Quartz grains vary widely in size and shape (Figure 3a, d–h). Coarse quartz ribbons (5–6 mm) exhibit a shape-preferred orientation (Figure 3a, b), whereas fine grains (100–200 μ m) are more randomly oriented (Figure 3b, e). Quartz ribbons lack undulose extinction and recrystallisation features (red arrows, Figure 3a, d). As grain size decreases, quartz grains become irregular, then rounded (red box, yellow arrow, Figure 3f). Fine-grained quartz often develops tapered, interconnected zones (yellow arrow, Figure 3g) and finger-like protrusions along plagioclase boundaries (red arrow, Figure 3g).

Biotite dominantly occurs along quartz–plagioclase interfaces (red arrows, Figure 3c, h) and commonly shows a consistent shape-preferred orientation (blue arrows, Figure 3c). Finer biotite grains, typically associated with fine anhedral quartz (yellow arrow, Figure 3h), are more randomly oriented and occasionally display bending without kinking (red arrow, Figure 3h).

Plagioclase forms a network-like framework throughout the sample (Figure 3b) and frequently develops finger-like apophyses that penetrate coarse quartz (black arrow, Figure 3b). Detailed examination reveals poikiloblastic textures, with fine quartz inclusions intergrown in coarse plagioclase patches (red arrows, Figure 3e, f).

Medium biotite mode (MM) sample

The MM sample is a schist consisting of biotite (37%; 0.5–4 mm), plagioclase (37%; 1–2 mm), quartz (18%; 1–2 mm), and minor garnet (<5%; \sim 1 mm; Figure 4). Compared with the LM sample, both quartz and plagioclase exhibit marked differences in grain shape, size, and texture. Notably, the proportion of quartz decreases significantly (to \sim 18%).

Plagioclase commonly forms cuspate grains and thin films along quartz or plagioclase boundaries (white arrows, Figure 4c). Interstitial plagioclase grains occur along quartz margins (purple arrow, Figure 4h), frequently displaying low dihedral angles against quartz (blue arrow, Figure 4h). Quartz is commonly elongate, with aspect ratios >8, and may occur as films enclosed within coarse biotite (red arrows, Figure 4f, g). These films connect to coarse, anhedral quartz grains with lobate plagioclase boundaries (Figure 4q).

Biotite occurs in two distinct textural groups. The first, Bta, consists of fine (<2 mm), well-aligned grains that define foliation (red arrows, Figure 4a, d). The second, Btb, comprises coarse (>2 mm), patchy grains with random orientation (yellow arrow, Figure 4a, e). While Bta dominates, Btb is locally concentrated and encloses well-faceted garnet grains (Figure 4e).

High biotite mode (HM) sample

The HM sample is mineralogically banded, consisting of alternating felsic (Qz–PI) and biotite–garnet–ilmenite (Bt–Gt–Ilm) bands (Figures 2f and 5). The overall modal composition is ~38% biotite, 20% quartz, 19% plagioclase, 16% garnet, 7% ilmenite, and trace apatite (<1%). However, biotite content locally increases to ~57% in the Bt–Gt–Ilm bands.

The Bt–Gt–Ilm bands contain biotite, garnet (18%), ilmenite (7%), and rare apatite (~2%). Biotite occurs as coarse, mm-scale grains aligned parallel to foliation and subparallel to banding (Figure 5a, b). Garnet displays bimodal grain sizes: finer euhedral grains (<500 µm) are abundant and evenly distributed, while coarse grains (2–3 mm, locally up to 3 cm) are rare (red arrow, Figure 5d). Many garnet grains exhibit rounded margins (Figure 5g) and may cluster into patches that host interstitial ilmenite with cuspate or lobate grain boundaries (red arrow, Figure 5g).

The Qz–PI (felsic) bands are dominated by coarse quartz (4–6 mm) and plagioclase (1–2 mm), with minor garnet (2–3 mm). Quartz grains lack undulose extinction or evidence of grain-size reduction (Figure 5e). Fine plagioclase grains commonly rim quartz (purple arrows, Figure 5f) and show interstitial habits or cuspate margins (Figure 5h). Minor biotite commonly occurs at quartz–plagioclase interfaces (yellow arrow, Figure 5h).

At band contacts, small garnet grains and aligned biotite occur (red arrows, Figures 5c, d and 6a). Biotite here is coarse, elongate, and free of deformation features such as undulose extinction or kinking (Figure 5d, g). Coarse biotite also forms apophyses with interstitial textures (yellow arrow, Figure 6b). Ilmenite is interstitial to garnet—biotite aggregates, aligned with foliation, and locally shows tapered margins against garnet (yellow arrow, Figure 6c).

Accessory phases include rare synchisite, identified during a search for monazite. Synchisite grains occur as patchy, LREE-carbonate replacements, possibly associated with thorite (white grains, yellow arrow, Figure 6d). Some synchisite partially replaces euhedral precursors (likely monazite or apatite; red arrow, Figure 6e).

Cathodoluminescence characteristics

Quartz and plagioclase grains, which appear relatively featureless in plane light, reveal internal complexities under cathodoluminescence (CL). In the MM sample, some plagioclase grains display variation in CL response. In Figure 7a, grains marked by red arrows show a brighter response (Figure 7b) compared to adjacent darker plagioclase grains (blue arrows, Figure 7a, b).

At the contact between the Bt–Gt–Ilm and Qz–Pl domains, quartz exhibits a gradational CL response. Coarse quartz grains (yellow arrow, Figure 7c) are the brightest (Figure 7d), while their margins and adjoining grains (blue arrows, above white dashed line, Figure 7d) show intermediate luminescence. Quartz grains in direct contact with biotite display a dark CL response (red arrow, Figure 7d).

Plagioclase grains along this band contact contain quartz blebs (red arrows, Figure 7e–g), where quartz forms low dihedral angles with plagioclase (yellow arrow, Figure 7g). Two of the three nearby plagioclase grains share a similar crystallographic orientation (green Euler colour, black arrows, Figure 7f), while the intervening grain differs (pale yellow–green). Notably, grains with similar Euler orientations also display similar CL responses (black arrows, Figure 7g).

Quantitative orientation analysis

In the LM sample, coarse quartz is surrounded by finer quartz and plagioclase (Figures 3a, e and 8a). The quartz inverse pole figure (IPF) orientation map shows random orientations throughout (Figure 8b). In contrast, the plagioclase orientation map reveals two textural types (Figure 8c). The first comprises small, subhedral grains in the upper part of the image (stippled white box, Figure 8c), which show variable orientations. The second comprises large poikiloblastic domains with a skeletal habit, exemplified by two grains at the base of the image (green and blue colours, Figure 8c, d). Although these domains appear fine-grained under plane polarised light (PPL) and resemble quartz in grain size (Figures 3a, e, f and 8a), orientation maps confirm they are networks of adjoining grains sharing similar orientations, representing single coarse poikiloblasts. Pole figures of plagioclase grains illustrate this clustering (Figure 8e). Although the data points in each cluster are tightly grouped, they show minor dispersion.

In the HM sample, crystallographic relationships differ markedly. The phase map (Figure 9a) shows the distribution of quartz, plagioclase, and coarse garnet in the felsic (Qz–Pl) band. A misorientation map of a coarse quartz grain (Figure 9b) reveals internal orientation variation of ~10° across 3 mm, with a reference orientation marked by a white cross. Adjacent, non-touching plagioclase grains (cluster 1, Figure 9c) share the same orientation (identical Euler colours), a relationship also reflected in c-axis pole figures (inset, Figure 9c). Another grain (grain 2) shows a distinct orientation. Plagioclase grains exhibit low dihedral angles and interstitial habits along quartz boundaries. Pole figures (Figure 9d) show weak crystallographic preferred orientation (CPO) in plagioclase, random orientations in quartz, and widely dispersed orientations in coarse garnet.

In the Bt–Gt–IIm band of the HM sample, garnet is abundant (Figure 10a). A medium-grained interstitial ilmenite grain shows limited internal deformation in its misorientation map (0–10°, green—white; Figure 10b), with the reference orientation marked by a white cross. The corresponding misorientation profile confirms minimal strain. The Euler map (Figure 10c) highlights variable orientations among adjoining fine-grained garnets, including one rare grain with a distinct core—rim orientation contrast (red arrow, Figure 10c). Pole figures (Figure 10d) show a strong CPO in ilmenite and biotite, possibly because ilmenite is hosted within biotite. In contrast, garnet grains are randomly oriented, similar to coarse garnet in the Qz–PI band.

Mineral chemistry

Major elements

Plagioclase compositions show systematic variation across the shear zone. In the LM sample, all analysed grains are chemically uniform, ranging from Ab15.3 to Ab17.7. In contrast, the MM sample displays broader variability, with albite contents from Ab33.9 to Ab47.3. The HM sample is the most albitic, ranging from Ab53.0 to Ab76.3. Overall, plagioclase becomes progressively more albitic from LM through MM to HM (Figure 11a).

The HM sample contains two distinct domains: (i) a quartz–plagioclase–rich leucosome band, and (ii) a biotite–garnet–ilmenite (Bt–Gt–Ilm) band (Figure 6). Within the Bt–Gt–Ilm band, rare fine-grained plagioclase–quartz intergrowths occur, with plagioclase compositions of Ab55–56 (yellow arrow, Figure 6a). In the adjacent Qz–Pl band, coarser plagioclase grains display weak chemical zoning, with slightly more albitic cores (red arrow, Figure 6a). Rim compositions overlap with those of finer-grained plagioclase in the Bt–Gt–Ilm domains (Ab55). Furthermore, CL imaging shows that darker-responding plagioclase (Figure 7g) is more albitic (Ab66) than brighter grains (Ab55, black arrow, Figure 7g).

Biotite compositions are plotted in a ternary classification diagram after Nachit *et al.* (2005) (Figure 11b). Grains from all samples cluster at the boundary between "re-equilibrated biotite" and "primary magmatic biotite." Notably, some grains from the HM sample plot fully within the primary magmatic field, consistent with a compositional trend from LM to HM.

Ti vs XMg systematics further illustrate this trend (Figure 11c). XMg decreases from 0.55 (LM) to 0.46 (HM), whereas Ti increases toward the HM sample. Conversely, Ti vs XFe shows an opposite

relationship: XFe rises from 0.44 (LM) to 0.47–0.49 (MM) and 0.48–0.53 (HM), with Ti again increasing in the HM sample (Figure 11d).

Garnet compositions also vary systematically. In ternary plots (Figure 11e), garnets from MM and HM form distinct clusters. HM garnets are slightly more enriched in almandine and spessartine than those from MM, though chemical variation between the two bands in HM is negligible. To further explore garnet chemistry, CaO vs MnO plots (after Harangi et al., 2001) were used. In all samples, CaO concentrations exceed MnO. However, garnets from MM contain higher CaO (~4 wt%), whereas those from HM have lower values (~3 wt%), indicating a systematic compositional shift. All garnets fall within the field of S-type magmatic crystallisation. Within-sample variability is limited in both MM and HM

Rare earth element chemistry of minerals

REE concentrations correlate with mineral microstructural context. Biotite shows the widest variability, spanning three orders of magnitude. In the LM sample, REE patterns are internally consistent (Figure 12a). In contrast, biotite from the MM sample displays marked heterogeneity, with profiles that intersect and diverge, particularly in Ce contents: some grains are strongly enriched, while others—especially coarse patchy biotite (Figure 4a)—are depleted. In the HM sample, biotite grains are depleted in HREE and exhibit diverging or intersecting patterns at the HREE end.

Garnet REE patterns are broadly similar between MM and HM samples, with slight HREE enrichment in HM. Some HM garnets are also Ce-enriched, particularly those at the contact between the Qz–PI and Bt–Gt–IIm bands (pink arrow, Figure 6a). In contrast, finer, randomly distributed garnet grains within the Bt–Gt–IIm bands are Ce-poor (white arrow, Figure 6a; Figure 12b).

Plagioclase REE chemistry shows the strongest contrasts. In the LM sample, most grains are LREE-poor, but a subset, corresponding to patchy grains identified in EBSD data (Figure 8), is distinctly LREE-enriched. MM plagioclase shows consistent subparallel REE patterns, with only minor variability. In the HM sample, approximately half of the grains are strongly LREE-enriched, with concentrations up to two orders of magnitude higher than all other plagioclase analysed (Figure 12c). These enriched grains also show REE profiles that intersect, particularly at the HREE end. CL imaging links REE enrichment to luminescence: darker CL domains (red dot, Figure 12d) are enriched in LREE and Gd relative to brighter domains (black, green, and blue dots).

Discussion

The microstructural and microchemical observations provide insights into the mineralogical and rheological evolution of the Cattle Water Pass shear zone. We evaluate the role of melt during deformation, the open-system behaviour associated with melt flux, and evidence for episodic melt pulses. Finally, we propose a model for the progressive widening of unusually thick biotite-rich shear zones in the Strangways Range.

Conditions at the time of shear localisation: melt presence and associated reactions

All samples preserve microstructural features diagnostic of former silicate melt (Daczko & Piazolo, 2022; Daczko *et al.*, 2025; Gardner *et al.*, 2024, 2025; Meek et al., 2019; Munnikhuis *et al.*, 2023; Stuart *et al.*, 2016, 2017, 2018a,b), with no evidence of low-temperature retrogression at thin-section scale. These include: (1) low dihedral angles in plagioclase (Figure 4c, h) and quartz (Figure 7g); (2) interstitial grains of plagioclase (Figures 4c, h and 5h), ilmenite (Figures 5g and 6c), and biotite (Figure 6b); (3) highly elongate quartz grains (aspect ratio > 8) along grain boundaries, interpreted as pseudomorphs of melt films (Figure 4f, g); and (4) "string-of-beads" textures of plagioclase along quartz boundaries, representing former melt pockets (Figure 5f; Holness & Sawyer, 2008).

Although the shear zone lacks classic leucosome geometry, these textures are consistent with crystallisation from intergranular melt (Brown & Solar, 1998; Daczko & Piazolo, 2022; Sawyer, 1994).

Additional evidence supports melt presence during deformation rather than post-tectonic infiltration. Quartz inclusions within foliation-defining biotite (Figure 4g), three-dimensional melt networks inferred from films around grains (Figure 9c), and low dihedral angles at triple junctions (Holness, 1997; Sawyer & Brown, 2008) all require syn-deformational melt. Such features would collapse or texturally re-equilibrate during static melt percolation (Holness, 2006). Adjacent plagioclase grains sharing identical Euler colours further suggest three-dimensional connectivity.

Poikiloblastic plagioclase with dispersed orientations (Figure 8d, e) indicates replacement reactions during melt percolation (Spruzeniece *et al.*, 2017). Together, these features show that deformation was accommodated in the presence of a connected melt network that facilitated ingress, reaction and egress of melt.

The LM sample, though closest to a granulite precursor, lacks classic felsic granulite features. It contains minor sillimanite (Figure 3h), low proportions of K-feldspar and garnet, no undulose extinction in quartz (Figure 3d), and melt-pseudomorph textures (Figure 3g). Finer plagioclase and quartz fingers intruding coarse quartz (Figure 3b) show that melt infiltration postdated coarse quartz growth. Poikiloblastic plagioclase with quartz inclusions (Figures 3e, f, and 8c) crystallised synkinematically from melt, contrasting with static metamorphic poikiloblasts. The inclusion distribution, cuspate boundaries, and alignment with coarse biotite foliation all support this interpretation. Patchy plagioclase textures (Figures 8c–e) reflect three-dimensional replacement networks, likely formed by melt replacing precursor K-feldspar.

The MM sample preserves similar melt-related features: low dihedral angles, interstitial plagioclase, and elongate quartz grains (Figures 4f–h, and 9c), but shows greater hydration, with abundant biotite defining foliation (Figure 4a, b). Two generations of biotite occur: foliated grains (Bta) formed by hydration reactions, and patchy, randomly oriented grains (Btb; Figure 4a, e) associated with garnet growth. The latter resemble leucosome-related bands (Handy *et al.*, 2001) and mark more extensive melt–rock interaction than in LM.

These microstructures imply that substantially more melt was present than is now preserved. Much of it likely migrated out during deformation, leaving behind biotite—garnet-rich residua (*cf.* Piazolo *et al.*, 2020; Silva *et al.*, 2022). Garnet nucleation and co-growth with biotite (Figure 5a, c) suggest melt-assisted crystallisation under supra-solidus conditions. The absence of subgrains and undulose extinction in quartz (Figures 5e and 9b) further supports deformation in melt-present conditions. Late plagioclase growth is evident from "string-of-beads" textures (Figure 5f), while EBSD data showing identical orientations in adjacent interstitial grains (Figure 9d) confirms crystallisation from melt.

In the HM sample, melt–rock interaction is even more advanced. Thick Bt–Gt–Ilm bands preserve biotite- and garnet-rich fabrics interpreted as former melt flux pathways. These resemble glimmerites and melferites described elsewhere (Daczko & Piazolo, 2022; Silva *et al.*, 2022) and are interpreted as cryptic records of transient melt pulses. Garnet trails align with biotite foliation (Figure 5c), suggesting rheologically weak zones were repeatedly reactivated during melt infiltration (Holdsworth *et al.*, 1997). Ilmenite textures (Figures 5g and 6c) reflect disequilibrium crystallisation and replacement, consistent with evolving melt compositions and episodic melt pulses. Garnet grain size correlates with local melt residence time: coarser grains with long-lived melt, finer grains with short-lived pulses (Figure 5d). These patterns match diffusion-limited growth models (Carlson, 2011; Konrad-Schmolke *et al.*, 2005) and recent field evidence for pulsed melt-assisted garnet recrystallisation (Hasalová *et al.*, 2008).

The regional context reinforces this interpretation. Pegmatites, felsic dykes, and leucosomes with biotite selvedges in the Alice Springs Orogen (Buick *et al.*, 2008; Piazolo *et al.*, 2020; Varga *et al.*, 2022) suggest external, hydrous S-type granitic melts (*e.g.* Jessop *et al.*, 2025) infiltrated granulite-facies basement. In our samples, the absence of hydrous breakdown textures, the irregular distribution of melt-related domains, and the coexistence of garnet with biotite support infiltration by externally derived melts, not *in situ* anatexis. Variations in melt composition, residence time, and reaction extent explain differences between this study and previous descriptions.

Biotite crystallised syn-tectonically from infiltrating melt, forming cuspate and interstitial aggregates along foliation and garnet margins (Figures 5c and 8b). Its lack of retrograde features (e.g. chlorite alteration) rules out post-tectonic hydration. Garnet, typically peritectic in migmatites, here occurs as relatively inclusion-free, subhedral grains, consistent with early syn-deformational crystallisation. Together, these textures reflect dynamic melt–rock interaction during ductile deformation, not static hydration or retrogression.

In summary, the microstructural record of the Cattle Water Pass shear zone is best explained by syn-deformational melt influx, reaction and egress. Episodic melt pulses drove mineralogical replacement, produced disequilibrium textures, and facilitated strain localisation through rheological weakening. Melt influx not only transformed granulite precursors into biotite—garnet-rich assemblages but also progressively widened the shear zone by repeatedly reactivating weak domains. Externally derived, hydrous S-type melts thus played a central role in shear zone evolution in the deep crust.

Melt present strain localisation: chemical signatures suggesting repeated open system behaviour

The chemical signatures observed across the samples point to repeated open-system behaviour. This interpretation is supported by variability in mineral chemistry both between the LM, MM, and HM samples, and within individual samples, together with associated reaction sequences.

From a geochemical perspective, the degree of variability is significant. Across the shear zone, the anorthite content of plagioclase shows a clear progression from LM to HM (Figure 11a), inconsistent with closed-system evolution. Such systematic variation requires external input, most plausibly an infiltrating fluid or melt that mobilised and redistributed elements at a regional scale. Increasingly albitic compositions in the HM sample suggest that higher melt–rock ratios enhanced chemical buffering, with the melt imposing its composition on the host rock. The enrichment of LREE in HM plagioclase grains (Figure 12c) scales with inferred melt abundance, whereas HREE enrichment is suppressed due to concurrent garnet growth, which sequestered HREE. Thus, plagioclase chemistry provides a sensitive proxy for the intensity of melt–rock interaction.

Biotite chemistry also records progressive melt buffering. From LM to HM, Fe content increases while Mg decreases (Figure 11c), and Ti shows a weak but systematic increase. These trends differ markedly from biotite produced during *in situ* partial melting, which typically shows heterogeneous zoning, reaction textures, and Fe–Ti depletion during melt extraction. Instead, HM biotite compositions plot closer to the "primary magmatic" field (Figure 11b), consistent with equilibration in the presence of an externally derived, hydrous granitic melt. Elevated Ti substitution in HM biotite (Figure 11d) further suggests higher crystallisation temperatures (Douce, 1993). Meanwhile, REE patterns are irregular and unsystematic across samples. Such behaviour is expected in open systems, as REEs are far more mobile in silicate melts than in aqueous fluids (Adam *et al.*, 2014). In contrast, equilibrium crystallisation of granulite-facies biotite normally yields systematic REE patterns reflecting partitioning with feldspar and garnet (Taylor *et al.*, 2015; White *et al.*, 2001). The lack of such patterns here reinforces the interpretation of melt-buffered modification, most strongly developed in the HM sample.

Garnet compositions further support melt influx and reaction. In MM and HM samples, garnet populations form distinct clusters (Figure 11e), with HM garnet enriched in almandine relative to MM. The HM garnet data plot centrally within the "S-type granite" field (Figure 11f), whereas MM garnet lies near the periphery. This suggests progressive equilibration with an infiltrating granitic melt, plausibly derived from sedimentary protoliths similar to those in the Harts Range (Maidment *et al.*, 2013). REE patterns in garnet from both samples are broadly similar, but HM garnet shows slightly elevated HREE (Figure 12b), again consistent with greater melt buffering under open-system conditions (Clarke *et al.*, 2013).

Within single samples, mineral-scale variability also records multiple stages of melt–rock interaction. In LM, poikiloblastic plagioclase is indistinguishable in major-element chemistry from finer grains but contains higher LREE (Figures 8d and 12c). This may reflect replacement of an LREE-rich precursor, likely K-feldspar. In MM, two chemical clusters of plagioclase (Figure 11a) correspond to contrasting CL responses (Figure 7a, b), suggesting interaction with melts of differing compositions. In HM, variability is even greater: plagioclase in the Qz–Pl band shows rims matching fine-grained plagioclase in adjacent Bt–Gt–Ilm bands (Figure 6a, arrows), indicating temporal changes in melt chemistry. REE data from HM plagioclase (Figures 8d and 12d) show cross-cutting and intersecting trends, best explained by multiple batches of melt with variable REE contents (Ague, 2017). Enhanced REE mobility in silicate melts compared with aqueous fluids (Adam *et al.*, 2014) accounts for these unsystematic patterns.

Quartz also preserves evidence of multiple melt ingress and reaction events. Gradational CL zoning in HM quartz (Figure 7c, d) does not correspond to grain boundaries, implying overprinting by successive melt-related processes. Although the precise sequence cannot be constrained without geochronology, the mismatches between CL domains and crystal boundaries support repeated modification by compositionally distinct melt pulses. This interpretation is consistent with the higher variability in REE chemistry of biotite and plagioclase in HM relative to LM and MM (Figure 12), which is uncommon in closed-system anatectic rocks but characteristic of open-system melt influx (Carvalho *et al.*, 2017).

Mineral reactions also support repeated episodes of melt–rock interaction. Monazite, commonly used to date Alice Springs Orogen deformation (Piazolo *et al.*, 2020), is absent from our samples. In contrast, nearby shear zones such as Gough Dam preserve monazite with highly variable ages (Silva *et al.*, 2022). In our samples, monazite appears to have been replaced by synchysite and

thorite (Figure 6d, e). Given that apatite remains unaltered, monazite is the more plausible precursor. Monazite breakdown during interaction with granitic melt, particularly in the presence of halogens, liberates REE and can produce synchysite (Förster, 2000, 2001; Varga et al., 2020). At least two stages of melt are therefore required: an early stage to crystallise monazite, and a later stage to replace it. Although an aqueous fluid could also trigger such reactions, the lack of retrograde textures and the widespread evidence for former melt argue instead for melt-driven monazite breakdown.

Taken together, the mineral chemistry, REE systematics, and replacement textures demonstrate repeated melt influx and open-system behaviour within the shear zone. The HM domain records the strongest modification, consistent with higher melt–rock ratios and multiple melt pulses progressively transforming the precursor granulite into biotite–garnet-rich shear zone assemblages.

Rheology of a melt-present shear zone: extensive softening caused by reaction and melt flux

Fluids play a fundamental role in deformation through two main mechanisms: (1) driving reactions that produce stronger or weaker minerals while interacting with other reactive fluids (Wibberley, 1999; Wintsch *et al.*, 1995), and (2) modifying the rheology of the fluid–rock mixture by inducing hydrofracturing or by weakening through the presence of melt (Bons *et al.*, 2012; Dijkstra *et al.*, 2003; Lee *et al.*, 2018; Rosenberg & Handy, 2005). Reaction-induced weakening or strengthening at the mineral scale influences the future strain history of the rock (Brodie & Rutter, 1985, 1987; Smith *et al.*, 2015; Wintsch & Dunning, 1985). Traditionally, reaction weakening is associated with the replacement of harder minerals by softer phases, such as phyllosilicates, particularly during retrogression, where it promotes strain localisation and the development of crustal-scale shear zones (Beach, 1980).

Grain size reduction within high-strain zones often accompanies fluid escape during dehydration reactions (Wibberley, 1999; Wintsch *et al.*, 1995, 2005). External fluids access reaction sites via microfractures formed during deformation (Yardley *et al.*, 2000). Consequently, retrograde microstructures appear patchy in low-strain regions but more pervasive in high-strain zones. Grain size reduction may occur either by recrystallisation or via reaction to form new minerals. In addition to mineral softening, the alignment of minerals develops a stronger CPO, which further weakens shear zone fabrics (Wintsch *et al.*, 1995).

Hydrofracturing or melt influx introduces veins and dykes, altering both the chemical and physical properties of the host rock, changing strain accommodation patterns and pore connectivity (Bons, 2001; Bons *et al.*, 2012; Dijkstra *et al.*, 2003; Etheridge *et al.*, 2021). Even a small fraction of melt significantly reduces rock strength (Vanderhaeghe, 2009). Organised and connected melt networks further weaken rock units and enhance creep rates (Kohlstedt & Zimmerman, 1996; Rosenberg & Handy, 2005), with >7 vol% melt potentially reducing rock strength by an order of magnitude (Rosenberg & Handy, 2005).

The shear zone studied here is defined by a schist belt containing hydrous assemblages that cut granulite-facies precursor rocks. A key feature is the variability in biotite modal abundance, with local processes contributing to metre-scale biotite-rich zones at the regional scale. Unlike retrogressed shear zones, biotite grains in highly modified samples remain coarse (Figures 5d and 6b), displaying distinctive interstitial textures (Figure 6b). Despite their size, these phyllosilicates still weaken the rock. Ilmenite grains, aligned with biotite and showing similar interstitial textures (Figures 6c and 10d), reinforce this weakening through their preferred orientation (Tommasi *et al.*, 2017). The observed CPO of biotite and ilmenite suggests syn-kinematic crystallisation, enhancing mechanical anisotropy, facilitating grain-boundary sliding, and promoting strain localisation in the presence of melt (Piazolo *et al.*, 2020; Silva *et al.*, 2022).

Plagioclase also shows preferred orientation in leucosome layers (Figure 9d), consistent with crystallisation in confined melt-rich zones. However, the lack of deformation microstructures in ilmenite and silicates (Figures 6c, 9c, and 10b) indicates that alignment and interstitial textures reflect melt presence rather than solid-state deformation (Daczko & Piazolo, 2022). Crystallisation of biotite, ilmenite, and garnet occurred during deformation, softening the rock fabric (Beard *et al.*, 2004; Tommasi *et al.*, 2017). Quartz films between aligned biotite grains (Figure 4g) and interstitial quartz at biotite—plagioclase contacts (Figure 4f) further support former melt along grain boundaries, marking former melt channels (Sawyer, 2001).

During melt ascent, melt initially accumulates at grain boundaries, then migrates along fabrics and fractures when deformation and melt flux are synchronous. Increasing pore connectivity allows the formation of vein networks (Brown *et al.*, 2011). Deformation promotes segregation and migration of melt through viscous grain-boundary sliding, pore formation, and ductile fracturing (Brown, 1994; Brown *et al.*, 2011). Grain-boundary melt enhances grain-boundary sliding and diffusion creep while

suppressing dislocation creep (Dell'Angelo *et al.*, 1987; Rosenberg & Handy, 2001). Dynamic cavity opening and closing ("porosity pump") further aid melt migration (Etheridge *et al.*, 2021; Fusseis *et al.*, 2009).

Melt–rock reactions that produce biotite weaken the rock by replacing stronger framework minerals, lowering viscosity, and promoting grain size reduction. These reactions facilitate grain-boundary sliding and dissolution–precipitation creep, contributing to CPO development in biotite and ilmenite. In addition, fine-grained garnet in Bt–Gt–Ilm bands of high biotite mode (HM) samples has reduced grain size relative to low biotite mode (LM) samples. Although not dynamic recrystallisation in the strict sense, this grain size reduction arises from high nucleation rates driven by melt infiltration (Skelton, 1997), promoting diffusion creep and grain-boundary sliding (Smith *et al.*, 2015). Garnet grains are randomly oriented and lack deformation features (Figure 10c, d), consistent with melt crystallisation. Their chemistry (Figure 11e, f) supports derivation from an S-type granitic melt (Harangi *et al.*, 2001).

Thus, structural, thermal, and chemical heterogeneities, all facilitated by external melt, contribute to shear zone softening. More broadly, melt–rock reactions may either weaken or transiently strengthen shear zones, depending on reaction products (e.g. hydrous vs harder minerals; Beard et al., 2004; Prakash et al., 2018). From mantle studies, even small melt fractions can reduce viscosity by a factor of 10 in fine-grained rocks (Kohlstedt & Zimmerman, 1996; Rosenberg & Handy, 2005). Melt enhances strain rates in both diffusion and dislocation creep regimes and melt redistribution may drive grain size reduction (Lee et al., 2018). Naturally deformed basement rocks thus record melt-assisted dislocation creep, diffusion-accommodated granular creep, and melt-induced veining. The interplay of these processes produces transient rheological changes.

Our observations support the broader concept that melt-present shear zones are key to facilitating intracontinental orogenesis in central Australia (Piazolo *et al.*, 2020).

Shear zone widening through pulsed melt flux: the Cattle Water Pass example

The Alice Springs Orogen is unusual among intracontinental orogens for its protracted activity, lasting over 150 million years (Raimondo *et al.*, 2014). Several distinct deformation phases have been linked to igneous intrusions (Buick *et al.*, 2008; Piazolo *et al.*, 2020). Despite this episodicity, the orogeny was characterised by a relatively constant differential stress regime (Raimondo *et al.*, 2014; Silva *et al.*, 2018) and sustained melt production (Piazolo *et al.*, 2020). Although cross-cutting relationships are not always preserved, prior work has argued that the episodic nature of the Alice Springs Orogen reflects repeated shear zone reactivation (Piazolo *et al.*, 2020 and references therein), an interpretation supported by extensive monazite, garnet, and mica geochronology (Cartwright *et al.*, 1999; Collins & Shaw, 1995; Raimondo *et al.*, 2014). Our microstructural and microchemical results from Cattle Water Pass are consistent with this multi-event history.

Patchy plagioclase grains in the LM sample invade and replace coarse quartz, indicating crystallisation from a melt influx after quartz formation. In the MM sample, two distinct biotite populations occur: differences in grain size, orientation, and association with garnet suggest two separate melt-related hydration events. Cathodoluminescence (CL) imaging further distinguishes older and younger quartz and plagioclase generations within the same sample, consistent with multiple episodes of melt ingress. In the HM sample, gradational CL responses across banded contacts (Figure 7d) and compositional variation in plagioclase (Figure 7f, g) likewise suggest repeated melt events. Garnet also records multistage growth: cores and rims differ in orientation (Figure 10c), and in some cases rims overprint earlier crystallisation. Finally, the absence of monazite, despite preservation of syncysite—thorite reaction textures, points to more than one episode of melt migration. Collectively, these features highlight repeated melt influx and shear zone reactivation.

Figure 13 illustrates a model of pulsed melt weakening. Two conditions may initiate deformation which can lead to melt ingress: (1) increased tectonic stress (*e.g.* plate reorganisation) or (2) elevated melt pressure overcoming rock strength. In our model, differential stress builds until fracturing occurs (Figure 13, strain gradient panel 1). Grain size reduction then increases surface area and porosity, allowing melt to infiltrate and wet grain boundaries. This transition promotes ductile behaviour: hydrous melts hydrate granulite into biotite-rich rock, while intergranular melt enhances grain-boundary sliding. Stress is thereby reduced as rocks soften.

Over time, shear zones may transiently harden through melt drainage, crystallisation of stronger minerals, and pore closure. Mancktelow (2002) demonstrated that pressure variations within shear zones depend on their kinematic evolution, with thinning zones exhibiting higher pressures than the host rock and thickening zones showing lower pressures. This pressure difference can drive melt

expulsion from the shear zone. Similarly, Oliot *et al.* (2014) noted that mean stress (or "pressure") gradients across shear zones promote fluid flow from actively deforming mylonites toward less deformed host rocks. Consistent with these findings, Finch *et al.* (2016) argued that variations in shear zone pressure or mean stress play a key role in controlling fluid migration between host rocks and shear zones.

Our model continues with a subsequent melt influx into the shear zone which lowers stress again, producing another weakening pulse. Repeated cycles of melt entry, weakening, drainage, and hardening progressively develop high-strain cores flanked by zones of moderate and low strain (Figure 13, strain gradient panel 2). Low strain to static dissolution—precipitation reactions occur at former weakened domains at the shear zone margins ("C" domains in Figure 13). These rheological interfaces act as weak zones that can be reactivated during later melt pulses (Gardner *et al.*, 2017).

Regional conditions also favour repeated melt flux. With geothermal gradients of 30–40 $^{\circ}$ C/km and pressures of $^{\circ}$ 6 kbar (Strangways Range) to $^{\circ}$ 9 kbar (Harts Range), mid-crustal temperatures likely reached 600–800 $^{\circ}$ C. Given granulite-facies solidi of $^{\circ}$ 650–700 $^{\circ}$ 50 $^{\circ}$ C, parts of the shear zone were probably at or slightly above the solidus. Local suprasolidus conditions would have facilitated melt migration along strain-localised pathways without significant crystallisation or thermal arrest.

Shear zone widening reflects both structural and chemical changes. Structurally, coarse quartz—feldspar aggregates are replaced by finer-grained biotite and garnet, and mineral alignments strengthen foliation. Chemically, granulite is hydrated into biotite-rich domains. Melt influx may also locally increase temperature, adding to rheological variability. Following initial melt-present deformation, subsequent crystallisation reduces strain localisation, preserving microstructures from earlier phases. However, weaker boundary zones between hardened shear zone cores and moderate to low strain partially modified granulite can localise later strain. New pulses of melt are localised into these weaker boundary zones and widen these, feeding back into further shear zone growth. Each successive melt pulse therefore reuses and expands the pre-existing shear zone margins, producing cumulative thickening.

This cyclical process explains why earlier microstructures are only partially obliterated: repeated melt–rock interaction selectively modifies, overprints, or preserves features depending on strain intensity and melt flux. Over time, this results in shear zones that record a stratified archive, from shear zone core to margins, of multiple deformation and melt migration events.

Conclusion

The unusually thick, biotite-rich shear zones of the Strangways Metamorphic Complex formed through the migration of silicate melt during the Alice Springs Orogeny. Melt migration generated pathways through precursor granulites, leaving diagnostic structural and chemical signatures. By tracing these features across the shear zone, we show that the degree of modification correlates with proximity to melt flux, while variable mineral chemistry indicates open-system melt migration.

Our results highlight the complexity of recognising shear zone activation by multiple pulses of melt. Nevertheless, we demonstrate that sequential melt influx and deformation drive progressive rheological change. We propose a model in which melt flux initially activates the shear zone core while low strain to static reactions occur in the shear zone margins. The first deformation cycle thus establishes a layered structure: highly modified cores, moderately to weakly modified boundary zones, and preserved granulite. Subsequent melt pulses partially reactivate the shear zone core and expand into the surrounding zones, with each cycle enlarging the intermediate strain layers through renewed melt-mediated dissolution—precipitation reactions.

This pulsed flux model accounts for the unusually high width-to-length ratios of Alice Springs Orogeny shear zones, attributing them to repeated cycles of melt-assisted failure, reactivation, and progressive widening, with strain preferentially localised along the margins of earlier shear zone events. In doing so, it provides a framework for understanding how syntectonic melt migration can drive both shear zone widening and the preservation of a multi-event deformation record.

Acknowledgements

We thank David Silva for assistance with fieldwork and sample collection. Tim Murphy (Macquarie University), Sandrin Feig (University of Tasmania), and Duncan Hedges (University of Leeds) provided valuable support during data acquisition at different stages of the project. Constructive reviews by Melanie Finch and Vasileios Chatzaras greatly improved the manuscript.

Disclosure statement

No potential conflict of interest was reported by the author(s).

Funding

This research was supported by ARC Discovery Project funding (DP160103449) awarded to T. R. and N. R. D.

ORCID

 H. Ghatak
 https://orcid.org/0000-0001-8998-033X

 N. R. Daczko
 https://orcid.org/0000-0002-3737-3818

 S. Piazolo
 https://orcid.org/0000-0001-7723-8170

 T. Raimondo
 https://orcid.org/0000-0001-9115-9196

Data availability statement

Data used in this study are contained in the Supplemental data (Tables ST1 to ST6).

References

- Adam, J., Locmelis, M., Afonso, J., Rushmer, T., & Fiorentini, M. (2014). The capacity of hydrous fluids to transport and fractionate incompatible elements and metals within the Earth's mantle. *Geochemistry, Geophysics, Geosystems*, *15*(6), 2241-2253. https://doi.org/10.1002/2013GC005199
- Ague, J. (2017). Element mobility during regional metamorphism in crustal and subduction zone environments with a focus on the rare earth elements (REE). *American Mineralogist*, 102(9). https://doi.org/10.2138/am-2017-6130
- Asimus, J. L., Daczko, N. R., & Ezad, I. S. (2023). Melt-present deformation at the Entia Dome, Central Australia: A metamorphic core complex formed during lower crustal tectonic extrusion. *Lithos*, 448, 107170. https://doi.org/10.1016/j.lithos.2023.107170
- Beach, A. (1980). Retrogressive metamorphic processes in shear zones with special reference to the Lewisian complex. *Journal of Structural Geology*, *2*(1-2), 257-263. https://doi.org/10.1016/0191-8141(80)90058-9
- Beard, J. S., Ragaland, P. C., & Rushmer, T. (2004). Hydration crystallization reactions between anhydrous minerals and hydrous melt to yield amphibole and biotite in igneous rocks: description and implications. *The Journal of Geology*, *112*(5), 617-621. https://doi.org/10.1086/422670
- Bendall, B. (2000). *Mid-Palaeozoic shear zones in the Strangways range: A record of intracratonic tectonism in the Arunta Inlier, central Australia* [unpublished PhD thesis]. University of Adelaide.
- Bestmann, M., & Prior, D. J. (2003). Intragranular dynamic recrystallization in naturally deformed calcite marble: diffusion accommodated grain boundary sliding as a result of subgrain rotation recrystallization. *Journal of Structural Geology*, 25(10), 1597-1613. https://doi.org/10.1016/S0191-8141(03)00006-3
- Bons, P. (2001). The formation of large quartz veins by rapid ascent of fluids in mobile hydrofractures. *Tectonophysics*, 336(1), 1-17. https://doi.org/10.1016/S0040-1951(01)00090-7
- Bons, P. D., Elburg, M. A., & Gomez-Rivas, E. (2012). A review of the formation of tectonic veins and their microstructures. *Journal of Structural Geology*, *43*, 33-62. https://doi.org/10.1016/j.jsg.2012.07.005
- Brodie, K. H., & Rutter, E. H. (1985). On the relationship between deformation and metamorphism, with special reference to the behavior of basic rocks. In *Metamorphic reactions: kinetics, textures, and deformation* (pp. 138-179). Springer New York.
- Brodie, K. H., & Rutter, E. H. (1987). The role of transiently fine-grained reaction products in syntectonic metamorphism: natural and experimental examples. *Canadian Journal of Earth Sciences*, 24(3), 556-564. https://doi.org/10.1139/e87-054
- Brown, M. (1994). The generation, segregation, ascent and emplacement of granite magma: the migmatite-to-crustally-derived granite connection in thickened orogens. *Earth-Science Reviews*, 36(1-2), 83-130. https://doi.org/10.1016/0012-8252(94)90009-4

- Brown, M., Korhonen, F. J., & Siddoway, C. S. (2011). Organizing melt flow through the crust. *Elements*, 7(4), 261-266. https://doi.org/10.2113/gselements.7.4.261
- Brown, M., & Solar, G. (1998). Shear-zone systems and melts: feedback relations and self-organization in orogenic belts. *Journal of Structural Geology*, 20(2-3), 211-227. https://doi.org/10.1016/S0191-8141(97)00068-0
- Buick, I., Storkey, A., & Williams, I. (2008). Timing relationships between pegmatite emplacement, metamorphism and deformation during the intra-plate Alice Springs Orogeny, central Australia. *Journal of Metamorphic Geology*, *26*(9), 915-936. https://doi.org/10.1111/j.1525-1314.2008.00794.x
- Bürgmann, R., & Dresen, G. (2008). Rheology of the lower crust and upper mantle: Evidence from rock mechanics, geodesy, and field observations. *Annual Review of Earth and Planetary Sciences*, *36*(1), 531-567. https://doi.org/10.1146/annurev.earth.36.031207.124326
- Byerlee, J. D. (1993). Model for episodic flow of high-pressure water in fault zones before earthquakes. *Geology*, 21(4), 303-306. https://doi.org/10.1130/0091-7613(1993)021%3C0303:MFEFOH%3E2.3.CO;2
- Carlson, W. D. (2011). Porphyroblast crystallization: linking processes, kinetics, and microstructures. *International Geology Review*, *53*(3-4), 406-445. https://doi.org/10.1080/00206814.2010.496184
- Cartwright, I., Buick, I., Foster, D., & Lambert, D. (1999). Alice Springs age shear zones from the southeastern Reynolds Range, central Australia. *Australian Journal of Earth Sciences*, 46, 355-363. https://doi.org/10.1046/j.1440-0952.1999.00710.x
- Carvalho, B. B., Sawyer, E. W., & Janasi, V. D. A. (2017). Enhancing maficity of granitic magma during anatexis: entrainment of infertile mafic lithologies. *Journal of Petrology*, *58*(7), 1333-1362. https://doi.org/10.1093/petrology/egx056
- Chatterjee, A., Daczko, N. R., Dey, J., & Piazolo, S. (2024). Hydrous shear zones are sites of melt transfer in the lower arc crust: A case study from Fiordland, New Zealand. *Journal of Metamorphic Geology*, *42*(7), 933-956. https://doi.org/10.1111/jmg.12788
- Clarke, G. L., Daczko, N. R., & Miescher, D. (2013). Identifying relic igneous garnet and clinopyroxene in eclogite and granulite, Breaksea Orthogneiss, New Zealand. *Journal of Petrology*, *54*(9), 1921-1938. https://doi.org/10.1093/petrology/egt036
- Collins, W., & Shaw, R. (1995). Geochronological constraints on orogenic events in the Arunta Inlier: a review. *Precambrian Research*, *71*, 315-346. https://doi.org/10.1016/0301-9268(94)00067-2
- Collins, W., & Teyssier, C. (1989). Crustal scale ductile fault systems in the Arunta Inlier, central Australia. *Tectonophysics*, 158(1), 49,60,63-58,60,66. https://doi.org/10.1016/0040-1951(89)90314-4
- Cyprych, D., Piazolo, S., Wilson, C. J., Luzin, V., & Prior, D. J. (2016). Rheology, microstructure and crystallographic preferred orientation of matrix containing a dispersed second phase: Insight from experimentally deformed ice. *Earth and Planetary Science Letters*, *449*, 272-281. https://doi.org/10.1016/j.epsl.2016.06.010
- D'Lemos, R. S., Schofield, D. I., Holdsworth, R. E., & King, T. R. (1997). Deep crustal and local rheological controls on the siting and reactivation of fault and shear zones, northeastern Newfoundland. *Journal of the Geological Society*, *154*(1), 117-121. https://doi.org/10.1144/gsjgs.154.1.0117
- Daczko, N., Piazolo, S., Meek, U., Stuart, C., & Elliott, V. (2016). Hornblendite delineates zones of mass transfer through the lower crust. *Scientific Reports*, *6*, 1-6. https://doi.org/10.1038/srep31369
- Daczko, N. R., & Piazolo, S. (2022). Recognition of melferite—A rock formed in syn-deformational high-strain melt-transfer zones through sub-solidus rocks: A review and synthesis of microstructural criteria. *Lithos*, *430*, 106850. https://doi.org/10.1016/j.lithos.2022.106850
- Daczko, N. R., Kamber, B. S., Gardner, R. L., Piazolo, S., & Cathey, H. E. (2025). Signatures of komatiite reactive melt flow through the Archaean Kaapvaal cratonic mantle. *Contributions to Mineralogy and Petrology*, 180(1), 5. https://doi.org/10.1007/s00410-024-02188-z
- Dell'Angelo, L. N., Tullis, J., & Yund, R. A. (1987). Transition from dislocation creep to melt-enhanced diffusion creep in fine-grained granitic aggregates. *Tectonophysics*, *139*(3-4), 325-332. https://doi.org/10.1016/0040-1951(87)90107-7
- Dijkstra, A. H., Barth, M. G., Drury, M. R., Mason, P. R., & Vissers, R. L. (2003). Diffuse porous melt flow and melt-rock reaction in the mantle lithosphere at a slow-spreading ridge: A structural petrology and LA-ICP-MS study of the Othris Peridotite Massif (Greece). *Geochemistry, Geophysics, Geosystems*, 4(8). https://doi.org/10.1029/2001GC000278

- Douce, A. E. P. (1993). Titanium substitution in biotite: an empirical model with applications to thermometry, O2 and H2O barometries, and consequences for biotite stability. *Chemical Geology*, 108(1-4), 133-162. https://doi.org/10.1016/0009-2541(93)90321-9
- Etheridge, M. A., Daczko, N. R., Chapman, T., & Stuart, C. A. (2021). Mechanisms of melt extraction during lower crustal partial melting. *Journal of Metamorphic Geology*, 39(1), 57-75. https://doi.org/10.1111/jmg.12561
- Finch, M. A., Weinberg, R. F., & Hunter, N. J. (2016). Water loss and the origin of thick ultramylonites. *Geology*, *44*(8), 599-602. https://doi.org/10.1130/G37972.1
- Förster, H. J. (2000). Cerite-(Ce) and thorian synchysite-(Ce) from the Niederbobritzsch granite, Erzgebirge, Germany: implications for the differential mobility of the LREE and Th during alteration. *The Canadian Mineralogist*, *38*(1), 67-79. https://doi.org/10.2113/gscanmin.38.1.67
- Förster, H. J. (2001). Synchysite-(Y)–synchysite-(Ce) solid solutions from Markersbach, Erzgebirge, Germany: REE and Th mobility during high-T alteration of highly fractionated aluminous A-type granites. *Mineralogy and Petrology*, 72(4), 259-280. https://doi.org/10.1007/s007100170019
- Fossen, H., & Cavalcante, G. C. G. (2017). Shear zones–A review. Earth-Science Reviews, 171, 434-455. https://doi.org/10.1016/j.earscirev.2017.05.002
- Fusseis, F., Handy, M. R., & Schrank, C. (2006). Networking of shear zones at the brittle-to-viscous transition (Cap de Creus, NE Spain). *Journal of Structural Geology*, 28(7), 1228-1243. https://doi.org/10.1016/j.jsg.2006.03.022
- Fusseis, F., Regenauer-Lieb, K., Liu, J., Hough, R. M., & De Carlo, F. (2009). Creep cavitation can establish a dynamic granular fluid pump in ductile shear zones. *Nature*, 459(7249), 974-977. https://doi.org/10.1038/nature08051
- Gardner, R., Piazolo, S., Evans, L., & Daczko, N. R. (2017). Patterns of strain localization in heterogeneous, polycrystalline rocks—a numerical perspective. *Earth and Planetary Science Letters*, 463, 253-265. https://doi.org/10.1016/j.epsl.2017.01.039
- Gardner, R. L., Piazolo, S., Daczko, N. R., & Trimby, P. (2020). Microstructures reveal multistage melt present strain localisation in mid-ocean gabbros. *Lithos*, *366*, 105572. https://doi.org/10.1016/j.lithos.2020.105572
- Gardner, R. L., Daczko, N. R., & Piazolo, S. (2024). The critical role of deformation-assisted melt migration in the formation of oceanic core complexes. *Australian Journal of Earth Sciences*, 71(1), 1-21. https://doi.org/10.1080/08120099.2023.2259451
- Gardner, R. L., Daczko, N. R., Piazolo, S., Adam, J., & Meek, U. (2025). Melt–rock Interaction experiments reveal rapid microstructural and chemical changes at lower crustal conditions. *Journal of Metamorphic Geology*, 43, 341-358. https://doi.org/10.1111/jmg.12811
- Ghatak, H., Gardner, R. L., Daczko, N. R., Piazolo, S., & Milan, L. (2022). Oxide enrichment by syntectonic melt-rock interaction. *Lithos*, *414*, 106617. https://doi.org/10.1016/j.lithos.2022.106617
- Ghatak, H., Daczko, N. R., Piazolo, S., & Raimondo, T. (2025). Fluid or Melt? Distinguishing Syn-Deformational Interaction Pathways. *Journal of Metamorphic Geology*, *43*(8), 810-838. https://doi.org/10.1111/jmg.70008
- Griffin, W., Powell, W., Pearson, N., & O'Reilly, S. (2008). GLITTER: data reduction software for laser ablation ICP-MS. In: Sylvester, P. (Ed.), *Laser Ablation- ICP-MS in the Earth Sciences* (pp. 204-207). Mineralogical Association of Canada Short Course Series. https://doi.org/10.3749/9780921294801.app02
- Hacker, B. R. (1997). Diagenesis and fault valve seismicity of crustal faults. *Journal of Geophysical Research: Solid Earth*, 102(B11), 24459-24467. https://doi.org/10.1029/97JB02025
- Haines, P. W., Hand, M., & Sandiford, M. (2001). Palaeozoic synorogenic sedimentation in central and northern Australia: a review of distribution and timing with implications for the evolution of intracontinental orogens. *Australian Journal of Earth Sciences*, *48*(6), 911-928. https://doi.org/10.1046/j.1440-0952.2001.00909.x
- Hand, M., & Sandiford, M. (1999). Intraplate deformation in central Australia, the link between subsidence and fault reactivation. *Tectonophysics*, *305*, 121-140. https://doi.org/10.1016/S0040-1951(99)00009-8
- Handy, M. R., Mulch, A., Rosenau, M., & Rosenberg, C. L. (2001). The role of fault zones and melts as agents of weakening, hardening and differentiation of the continental crust: a synthesis. In: Holdsworth, R.E., Magloughlin, J., Knipe, R.J., Strachan, R.A. & Searle, R.C. (Eds), *The Nature and Tectonic Significance of Fault Zone Weakening* (pp. 305-332). Geological Society, London, Special Publication, 186. https://doi.org/10.1144/GSL.SP.2001.186.01.18

- Harangi, S. Z., Downes, H., Kósa, L., Szabo, C. S., Thirlwall, M. F., Mason, P. R. D., & Mattey, D. (2001). Almandine garnet in calc-alkaline volcanic rocks of the Northern Pannonian Basin (Eastern–Central Europe): Geochemistry, petrogenesis and geodynamic implications. *Journal of Petrology*, 42(10), 1813-1843. https://doi.org/10.1093/petrology/42.10.1813
- Hasalova, P., Schulmann, K., Lexa, O., Stipska, P., Hrouda, F., Ulrich, S., . . . Tycova, P. (2008). Origin of migmatites by deformation-enhanced melt infiltration: A new model based on quantitative microstructural analysis. *Journal of Metamorphic Geology*, *26*, 29-53. https://doi.org/10.1111/j.1525-1314.2007.00743.x
- Hobbs, B. E., Ord, A., Spalla, M. I., Gosso, G., & Zucali, M. (2010). The interaction of deformation and metamorphic reactions. *Geological Society, London, Special Publications, 332*, 189–223. https://doi.org/10.1144/sp332.12
- Holdsworth, R. E., Butler, C. A., & Roberts, A. M. (1997). The recognition of reactivation during continental deformation. *Journal of the Geological Society*, *154*(1), 73-78. https://doi.org/10.1144/gsjgs.154.1.0073
- Holdsworth, R., Stewart, M., Imber, J., & Strachan, R. (2001). The structure and rheological evolution of reactivated continental fault zones: a review and case study. *Geological Society, London, Special Publications*, 184, 115-137. https://doi.org/10.1144/GSL.SP.2001.184.01.07
- Holness, M. B. (1997). Surface chemical controls on pore-fluid connectivity in texturally equilibrated materials. In: Jamtveit B. and Yardley B. W. D. (Eds), *Fluid flow and transport in rocks:*Mechanisms and effects (pp. 149-169). Chapman and Hall. https://doi.org/10.1007/978-94-009-1533-6 9
- Holness, M. B. (2006). Melt–solid dihedral angles of common minerals in natural rocks. *Journal of Petrology*, 47(4), 791-800. https://doi.org/10.1093/petrology/egi094
- Holness, M., & Clemens, J. (1999). Partial melting of the Appin Quartzite driven by fracture-controlled H2O infiltration in the aureole of the Ballachulish Igneous Complex, Scottish Highlands. *Contributions to Mineralogy and Petrology*, *136*, 154-168. https://doi.org/10.1007/s004100050529
- Holness, M. B., & Sawyer, E. W. (2008). On the pseudomorphing of melt-filled pores during the crystallization of migmatites. *Journal of Petrology*, *49*(7), 1343-1363. https://doi.org/10.1093/petrology/egn028
- Holness, M., Cesare, B., & Sawyer, E. (2011). Melted Rocks under the microscope: Microstructures and their interpretation. *Elements*, 7, 247-252. https://doi.org/10.2113/gselements.7.4.247
- Holyoke, C., & Tullis, J. (2006). The interaction between reaction and deformation: an experimental study using a biotite + plagioclase + quartz gneiss. *Journal of Metamorphic Petrology*, 24(8), 743-762. https://doi.org/10.1111/j.1525-1314.2006.00666.x
- Hull, J. (1988). Thickness-displacement relationships for deformation zones. *Journal of Structural Geology*, 10(4), 431-435. https://doi.org/10.1016/0191-8141(88)90020-X
- Jessop, K., Daczko, N. R., & Piazolo, S. (2025). Occurrence and petrogenesis of diverse S-type granites in an extensional tectonic setting: a case study from the Wongwibinda Complex, eastern Australia. *Australian Journal of Earth Sciences*, 72(2), 213-232. https://doi.org/10.1080/08120099.2025.2476519
- Ji, S., Wang, Z., & Wirth, R. (2001). Bulk flow strength of forsterite—enstatite composites as a function of forsterite content. *Tectonophysics*, *341*(1-4), 69-93. https://doi.org/10.1016/S0040-1951(01)00191-3
- Kohlstedt, D. L., & Zimmerman, M. E. (1996). Rheology of partially molten mantle rocks. *Annual Review of Earth and Planetary Sciences*, 24(1), 41-62. https://doi.org/10.1146/annurev.earth.24.1.41
- Konrad-Schmolke, M., Handy, M. R., Babist, J., & O'Brien, P. J. (2005). Thermodynamic modelling of diffusion-controlled garnet growth. *Contributions to Mineralogy and Petrology*, 149(2), 181-195. https://doi.org/10.1007/s00410-004-0643-6
- Lee, A. L., Torvela, T., Lloyd, G. E., & Walker, A. M. (2018). Melt organisation and strain partitioning in the lower crust. *Journal of Structural Geology*, *113*, 188-199. https://doi.org/10.1016/j.jsg.2018.05.016
- Lee, A. L., Lloyd, G. E., Torvela, T., & Walker, A. M. (2020). Evolution of a shear zone before, during and after melting. *Journal of the Geological Society*, 177(4), 738-751. https://doi.org/10.1144/igs2019-114
- Maidment, D., Hand, M., & Williams, I. (2005). Tectonic cycles in Strangways Metamorphic Complex, Arunta Inlier, central Australia: geochronological evidence for exhumation and basin formation between two high-grade metamorphic events. *Australian Journal of Earth Sciences*, *52*, 205-215. https://doi.org/10.1080/08120090500139414

- Maidment, D., Hand, M., & Williams, I. (2013). High grade metamorphism of sedimentary rocks during Palaeozoic rift basin formation in central Australia. *Gondwana Research*, 24(3-4), 865-885. https://doi.org/10.1016/j.gr.2012.12.020
- Mancktelow, N. S. (2002). Finite-element modelling of shear zone development in viscoelastic materials and its implications for localisation of partial melting. *Journal of Structural Geology*, 24(6-7), 1045-1053. https://doi.org/10.1016/S0191-8141(01)00090-6
- Martin, A. J., DeCelles, P. G., Gehrels, G. E., Patchett, P. J., & Isachsen, C. (2005). Isotopic and structural constraints on the location of the Main Central thrust in the Annapurna Range, central Nepal Himalaya. *Geological Society of America Bulletin*, 117(7-8), 926-944. https://doi.org/10.1130/B25646.1
- McDonough, W., & Sun, S. (1995). The composition of the Earth. *Chemical Geology*, 120(3-4), 223-253. https://doi.org/10.1016/0009-2541(94)00140-4
- Means, W. D. (1984). Shear zones of types I and II and their significance for reconstruction of rock history. Geological Society of America, Abstract with Programs, 16, 50.
- Means, W. D. (1995). Shear zones and rock history. *Tectonophysics*, 247(1-4), 157-160. https://doi.org/10.1016/0040-1951(95)98214-H
- Meek, U., Piazolo, S., & Daczko, N. R. (2019). The field and microstructural signatures of deformation-assisted melt transfer: Insights from magmatic arc lower crust, New Zealand. *Journal of Metamorphic Geology*, 37(6), 795-821. https://doi.org/10.1111/jmg.12488
- Mugnier, J. L., Huyghe, P., Leturmy, P., & Jouanne, F. (2004). Episodicity and rates of thrust-sheet motion in the Himalayas (western Nepal). In K. R. McClay (Ed.), Thrust tectonics and hydrocarbon systems (pp. 91-114). AAPG Memoir 82. https://archives.datapages.com/data/specpubs/memoir82/CHAPTER6/CHAPTER6.HTM
- Munnikhuis, J. K., Daczko, N. R., & Langone, A. (2023). Open system reaction between hydrous melt and gabbroic rock in the Finero Mafic Complex. *Lithos*, *440*, 107027. https://doi.org/10.1016/j.lithos.2023.107027
- Nachit, H., Ibhi, A., & Ohoud, M. B. (2005). Discrimination between primary magmatic biotites, reequilibrated biotites and neoformed biotites. *Comptes Rendus Géoscience*, 337(16), 1415-1420. https://doi.org/10.1016/j.crte.2005.09.002
- Norman, A. (1991). The structural and metamorphic evolution of the central Arunta Block: evidence from the Strangways Metamorphic Complex and the Harts Range Group, central Australia [unpublished PhD thesis]. Macquarie University.
- Oliot, E., Goncalves, P., Schulmann, K., Marquer, D., & Lexa, O. (2014). Mid-crustal shear zone formation in granitic rocks: Constraints from quantitative textural and crystallographic preferred orientations analyses. *Tectonophysics*, *612*, 63-80. https://doi.org/10.1016/j.tecto.2013.11.032
- Passchier, C. W., & Trouw, R. A. (2005). Microtectonics. Springer Science & Business Media.
 Piazolo, S., Daczko, N. R., Silva, D., & Raimondo, T. (2020). Melt-present shear zones enable intracontinental orogenesis. *Geology*, 48(7), 643-648. https://doi.org/10.1130/G47126.1
- Prakash, A., Piazolo, S., Saha, L., Bhattacharya, A., Pal, D. K., & Sarkar, S. (2018). Deformation behavior of migmatites: insights from microstructural analysis of a garnet–sillimanite–mullite–quartz–feldspar-bearing anatectic migmatite at Rampura–Agucha, Aravalli–Delhi Fold Belt, NW India. *International Journal of Earth Sciences*, 107(6), 2265-2292. https://doi.org/10.1007/s00531-018-1598-6
- Raimondo, T., Clark, C., Hand, M., & Faure, K. (2011). Assessing the geochemical and tectonic impacts of fluid–rock interaction in mid-crustal shear zones: a case study from the intracontinental Alice Springs Orogen, central Australia. *Journal of Metamorphic Geology*, 29, 821-850. https://doi.org/10.1111/j.1525-1314.2011.00944.x
- Raimondo, T., Hand, M., & Collins, W. (2014). Compressional intracontinental orogens: Ancient and modern perspectives. *Earth-Science Reviews*, *130*, 128-153. https://doi.org/10.1016/j.earscirev.2013.11.009
- Renner, J., Evans, B., & Hirth, G. (2000). On the rheologically critical melt fraction. *Earth and Planetary Science Letters*, 181(4), 585-594. https://doi.org/10.1016/S0012-821X(00)00222-3
- Rosenberg, C. L., & Handy, M. R. (2001). Mechanisms and orientation of melt segregation paths during pure shearing of a partially molten rock analog (norcamphor–benzamide). *Journal of Structural Geology*, 23(12), 1917-1932. https://doi.org/10.1016/S0191-8141(01)00037-2
- Rosenberg, C. L., & Handy, M. R. (2005). Experimental deformation of partially melted granite revisited: implications for the continental crust. *Journal of Metamorphic Geology*, 23(1), 19-28. https://doi.org/10.1111/j.1525-1314.2005.00555.x

- Rutter, E., & Neumann, D. (1995). Experimental deformation of partially molten Westerly granite under fluid-absent conditions, with implications for the extraction of granitic magmas. *Journal of Geophysical Research: Solid Earth*, 100(B8), 15697-1571. https://doi.org/10.1029/94JB03388
- Rybacki, E., & Dresen, G. (2004). Deformation mechanism maps for feldspar rocks. *Tectonophysics*, 382(3-4), 173-187. https://doi.org/10.1016/J.TECTO.2004.01.006
- Sawyer, E. W. (1994). Melt segregation in the continental crust. *Geology*, 22(11), 1019-1022. https://doi.org/10.1130/0091-7613(1994)022%3C1019:MSITCC%3E2.3.CO;2
- Sawyer, E. W. (2001). Melt segregation in the continental crust: distribution and movement of melt in anatectic rocks. *Journal of Metamorphic Geology*, *19*(3), 291-309. https://doi.org/10.1046/j.0263-4929.2000.00312.x
- Sawyer, E. W., & Brown, M. (2008). *Working with migmatites*. Mineralogical Association of Canada. Schelling, D., & Arita, K. (1991). Thrust tectonics, crustal shortening, and the structure of the fareastern Nepal Himalaya. *Tectonics*, *10*(5), 851-862. https://doi.org/10.1029/91TC01011
- Sibson, R. H. (1977). Fault rocks and fault mechanisms. *Journal of the Geological Society*, 133(3), 191-213. https://doi.org/10.1144/gsjgs.133.3.0191
- Sibson, R. H. (1990). Conditions for fault-valve behaviour. *Geological Society, London, Special Publications*, 54, 15-28. https://doi.org/10.1144/GSL.SP.1990.054.01.02
- Sibson, R. H. (1995). Selective fault reactivation during basin inversion: potential for fluid redistribution through fault-valve action. *Geological Society, London, Special Publications*, 88(1), 3-19. https://doi.org/10.1144/GSL.SP.1995.088.01.02
- Silva, D., Piazolo, S., Daczko, N. R., Houseman, G., Raimondo, T., & Evans, L. (2018). Intracontinental orogeny enhanced by far-field extension and local weak crust. *Tectonics*, 37(12), 4421-4443. https://doi.org/10.1029/2018TC005106
- Silva, D., Daczko, N. R., Piazolo, S., & Raimondo, T. (2022). Glimmerite: A product of melt-rock interaction within a crustal-scale high-strain zone. *Gondwana Research*, *105*, 160-184. https://doi.org/10.1016/j.gr.2021.09.005
- Silva, D., Piazolo, S., & Daczko, N. R. (2023). Trapped K-feldspar phenocrysts as a signature of melt migration pathways within active high-strain zones. *Journal of Metamorphic Geology*, *41*(3), 351-375. https://doi.org/10.1111/JMG.12698
- Simpson, C. (1985). Deformation of granitic rocks across the brittle-ductile transition. *Journal of Structural Geology*, 7(5), 503-511. https://doi.org/10.1016/0191-8141(85)90023-9
- Skelton, A. D. L. (1997). The effect of metamorphic fluid flow on the nucleation and growth of garnets from Troms, North Norway. *Journal of Metamorphic Geology*, *15*(1), 85-92. https://doi.org/10.1111/j.1525-1314.1997.t01-1-00051.x
- Smith, J. R., Piazolo, S., Daczko, N. R., & Evans, L. (2015). The effect of pre-tectonic reaction and annealing extent on behaviour during subsequent deformation: Insights from paired shear zones in the lower crust of Fiordland, New Zealand. *Journal of Metamorphic Geology*, 33(6), 557-577. https://doi.org/10.1002/2015GC006236
- Spruzeniece, L., Piazolo, S., & Maynard-Casely, H. E. (2017). Deformation-resembling microstructure created by fluid-mediated dissolution–precipitation reactions. *Nature Communications*, *8*(1), 14032. https://doi.org/10.1038/ncomms14032
- Stewart, M., Holdsworth, R. E., & Strachan, R. A. (2000). Deformation processes and weakening mechanisms within the frictional–viscous transition zone of major crustal-scale faults: insights from the Great Glen Fault Zone, Scotland. *Journal of Structural Geology*, 22(5), 543-560. https://doi.org/10.1016/S0191-8141(99)00164-9
- Stuart, C., Piazolo, S., & Daczko, N. (2016). Mass transfer in the lower crust: Evidence for incipient melt assisted flow along grain boundaries in the deep arc granulites of Fiordland, New Zealand. *Geochemistry, Geophysics, Geosystems*, 17, 3733-3753. https://doi.org/10.1002/2015GC006236
- Stuart, C., Daczko, N., & Piazolo, S. (2017). Local partial melting of the lower crust triggered by hydration through melt-rock interaction: an example from Fiordland, New Zealand. *Journal of Metamorphic Geology*, *35*, 213-230. https://doi.org/10.1111/JMG.12229
- Stuart, C., Daczko, N., & Piazolo, S. (2018a). The recognition of former melt flux through high-strain zones. *Journal of Metamorphic Geology*, *36*(8), 1049-1069. https://doi.org/10.1111/jmg.12427
- Stuart, C., Meek, U., Daczko, N., Piazolo, S., & Huang, J. (2018b). Chemical signatures of melt–rock interaction in the root of a magmatic arc. *Journal of Petrology*, *59*(2). https://doi.org/10.1093/petrology/egy029
- Taylor, R. J. M., Harley, S. L., Hinton, R. W., Elphick, S., Clark, C., & Kelly, N. M. (2015). Experimental determination of REE partition coefficients between zircon, garnet and melt: A key to

- understanding high-T crustal processes. *Journal of Metamorphic Geology*, 33(3), 231-248. https://doi.org/10.1111/jmg.12118
- Tetley, M. G., & Daczko, N. R. (2014). Virtual Petrographic Microscope: A multi-platform education and research software tool to analyse rock thin sections. *Australian Journal of Earth Sciences*, *61*, 631-637. https://doi.org/10.1080/08120099.2014.886624
- Teyssier, C. (1985). A crustal thrust system in an intracratonic tectonic environment. *Journal of Structural Geology*, 7(6), 689-700. https://doi.org/10.1016/0191-8141(85)90144-0
- Tommasi, A., Langone, A., Padron-Navarta, J. A., Zanetti, A., & Vauchez, A. (2017). Hydrous melts weaken the mantle, crystallization of pargasite and phlogopite does not: Insights from a petrostructural study of the Finero peridotites, southern Alps. *Earth and Planetary Science Letters*, 477, 59-72. https://doi.org/10.1016/j.epsl.2017.08.015
- Van der Molen, I., & Paterson, M. (1979). Experimental deformation of partially-melted granite. Contributions to Mineralogy and Petrology, 70, 299-318. https://doi.org/10.1007/BF00375359
- Vanderhaeghe, O. (2009). Migmatites, granites and orogeny: Flow modes of partially-molten rocks and magmas associated with melt/solid segregation in orogenic belts. *Tectonophysics*, 477(3-4), 119-134. https://doi.org/10.1016/j.tecto.2009.06.021
- Varga, J., Raimondo, T., Daczko, N. R., & Adam, J. (2020). Experimental alteration of monazite in granitic melt: Variable U–Th–Pb and REE mobility during melt-mediated coupled dissolution-precipitation. *Chemical Geology, 544*, 119602. https://doi.org/10.1016/j.chemgeo.2020.119602
- Varga, J., Raimondo, T., Hand, M., Curtis, S., & Daczko, N. (2022). Hydration, melt production and rheological weakening within an intracontinental gneiss dome. *Lithos*, *4*32, 106872. https://doi.org/10.1016/J.LITHOS.2022.106872
- Wallace, R. E. (1984). Patterns and timing of late Quaternary faulting in the Great Basin province and relation to some regional tectonic features. *Journal of Geophysical Research: Solid Earth*, 89(B7), 5763-5769. https://doi.org/10.1029/JB089iB07p05763
- Wallis, D., Lloyd, G. E., Phillips, R. J., Parsons, A. J., & Walshaw, R. D. (2015). Low effective fault strength due to frictional-viscous flow in phyllonites, Karakoram Fault Zone, NW India. *Journal of Structural Geology*, 77, 45-61. https://doi.org/10.1016/j.jsg.2015.05.010
- Wallis, D., Phillips, R. J., & Lloyd, G. E. (2013). Fault weakening across the frictional-viscous transition zone, Karakoram Fault Zone, NW Himalaya. *Tectonics*, 32(5), 1227-1246. https://doi.org/10.1002/tect.20076
- Weinberg, R. F., & Hasalová, P. (2015). Water-fluxed melting of the continental crust: a review. *Lithos*, 212, 158-188. https://doi.org/10.1016/j.lithos.2014.08.021
- White, S. T., & Knipe, R. J. (1978). Transformation-and reaction-enhanced ductility in rocks. *Journal of the Geological Society*, 135(5), 513-516. https://doi.org/10.1144/gsjgs.135.5.0513
- White, R., Powell, R., & Holland, T. (2001). Calculation of partial melting equilibria in the system Na2O-CaO-K2O-FeO-MgO-Al2O3-SiO2-H2O (NCKFMASH). *Journal of Metamorphic Geology*, 19(2), 139-153. https://doi.org/10.1046/j.0263-4929.2000.00303.x
- Whitney, D., & Evans, B. (2010). Abbreviations for the names of rock-forming minerals. *American Mineralogist*, 95, 185-187. https://doi.org/10.2138/am.2010.3371
- Wibberley, C. (1999). Are feldspar-to-mica reactions necessarily reaction-softening processes in fault zones? *Journal of Structural Geology*, *21*(8-9), 1219-1227. https://doi.org/10.1016/S0191-8141(99)00019-X
- Wintsch, R., & Dunning, J. (1985). The effect of dislocation density on the aqueous solubility of quartz and some geologic implications: a theoretical approach. *Journal of Geophysical Research*, 90(B5), 3649-3657. https://doi.org/10.1029/JB090iB05p03649
- Wintsch, R., Christoffersen, R., & Kronenberg, A. (1995). Fluid-rock reaction weakening of fault zones. *Journal of Geophysical Research*, 100(B7), 13021-13032. https://doi.org/10.1029/94JB02622
- Wintsch, R. P., Aleinikoff, J. N. & Yi, K. (2005). Foliation development and reaction softening by dissolution and precipitation in the transformation of granodiorite to orthogneiss, Glastonbury Complex, Connecticut, U.S.A. *Canadian Mineralogist*, *43*(1), 327-347. https://doi.org/10.2113/gscanmin.43.1.327
- Yakymchuk, C., & Brown, M. (2014). Consequences of open-system melting in tectonics. *Journal of the Geological Society*, 171(1), 21-40. https://doi.org/10.1144/jgs2013-039
- Yardley, B., Gleeson, S., Bruce, S., & Banks, D. (2000). Origin of retrograde fluids in metamorphic rocks. *Journal of Geochemical Exploration*, 69, 281-285. https://doi.org/10.1016/S0375-6742(00)00132-1
- Yardley, B. (2009). The role of water in the evolution of the continental crust. *Journal of the Geological Society*, *166*, 585-600. https://doi.org/10.1144/0016-76492008-101

Zhang, Y., Underschultz, J. R., Gartrell, A., Dewhurst, D. N., & Langhi, L. (2011). Effects of regional fluid pressure gradients on strain localisation and fluid flow during extensional fault reactivation. Marine and Petroleum Geology, 28(9), 1703-1713. https://doi.org/10.1016/j.marpetgeo.2011.07.006

Figure captions

- **Figure 1.** Geological context of the study area. (a) Regional geological map of the Arunta region showing the granulite facies Strangways Metamorphic Complex (SMC, pink) and Harts Range Group (brown) among amphibolite facies (purple) rocks, both cut by schistose high strain zones and anastomosing thrust shear zones (green) in central Australia (after Silva *et al.*, 2018). The black square indicates the sample area at Cattle Water Pass. Yellow-green stippled pattern are rocks of the covering Georgina (north) and Amadeus (south) basins. (b) Detailed outcrop map of the Cattle Water Pass shear zone showing foliation trajectories (lines) and sample locations selected from a single outcrop of variably modified precursor granulite.
- **Figure 2.** Outcrop images and thin-section blocks of the three samples investigated. (a) Outcrop of the 'low biotite mode' (LM) sample CP1604A. (b) Outcrop of the 'medium biotite mode' (MM) sample CP1604B, showing anastomosing biotite-rich bands. (c) Outcrop of the leucosome and 'high biotite mode' (HM) domains, rich in biotite and garnet, in sample CP1604C. (d) Thin-section block of the LM sample with low biotite content (10%). (e) Thin-section block of the MM sample with patchily distributed biotite (37%). (f) Thin-section block comprising a leucosome domain and an HM domain rich in biotite (57%).
- **Figure 3.** Petrographic and microstructural observations in the LM sample (CP1604A). (a) Crosspolarised light (XPL) overview of the thin section showing a bimodal grain-size distribution and abundant quartz. (b) Micro-XRF phase map showing quartz and plagioclase; black arrows highlight poikiloblastic plagioclase fingers invading quartz. (c–h) Photomicrographs (PPL, XPL) and backscattered electron (BSE) images: (c) biotite at quartz–plagioclase boundaries (red arrow), with grains commonly aligned (blue arrows); (d) coarse quartz lacking undulose extinction (red arrow); (e) poikiloblastic plagioclase with quartz inclusions (red arrows); (f) gradational quartz grain size from fine in the plagioclase core (yellow arrow) to coarser at the rim; (g) melt pseudomorph textures, including connected grains (yellow arrow) and cuspate shapes (red arrow); (h) curved biotite (red arrow) moulding adjacent quartz and plagioclase. Rare sillimanite also present.
- **Figure 4.** Petrographic and microstructural observations in the MM sample (CP1604B). (a) Plane-polarised light (PPL) overview showing biotite distribution and rare garnet (inset). (b) Micro-XRF phase map highlighting abundant biotite. (c–h) Photomicrographs (PPL, XPL) and BSE images: (c) interstitial plagioclase film along quartz–biotite boundaries (white arrow); (d) biotite (Bt_a) defining foliation; (e) coarse, patchy, randomly oriented biotite (Bt_b); (f) interstitial quartz film at biotite–plagioclase boundaries (red arrow); (g) interstitial quartz film between two biotite grains (red arrow); (h) irregular plagioclase with protrusions forming boundary films (purple arrow) or terminating at low dihedral angles (blue arrow).
- **Figure 5.** Petrographic and microstructural observations of leucosome and HM domains in sample CP1604C. (a) PPL overview showing banded domains. (b) Micro-XRF phase map highlighting quartz—plagioclase-rich leucosome and ilmenite-rich garnet—biotite domain. (c—h) Photomicrographs (PPL, XPL) and BSE images: (c) garnet aggregates (red arrow) associated with biotite; (d) coarse garnet associated with coarse biotite (red arrow), fine garnet with fine biotite (blue arrow); (e) coarse quartz lacking undulose extinction; (f) "string of beads" plagioclase along quartz boundaries (purple arrows); (g) interstitial ilmenite (green arrow) between garnet grains, partly replacing garnet (red arrow); (h) interstitial plagioclase film (purple arrow) along quartz—biotite boundaries (yellow arrow).
- **Figure 6.** Back-scattered electron images of sample CP1604C. (a) Boundaries between leucosome and HM domains (Bt–Grt–Ilm band) marked by dashed lines. Arrows indicate: plagioclase in Bt+Grt+Ilm band (yellow), garnet with relatively higher Ce at contact zone (pink), zoned plagioclase in leucosome (red), and garnet with lower Ce in Bt+Grt+Ilm band (white). (b) Two biotite grains

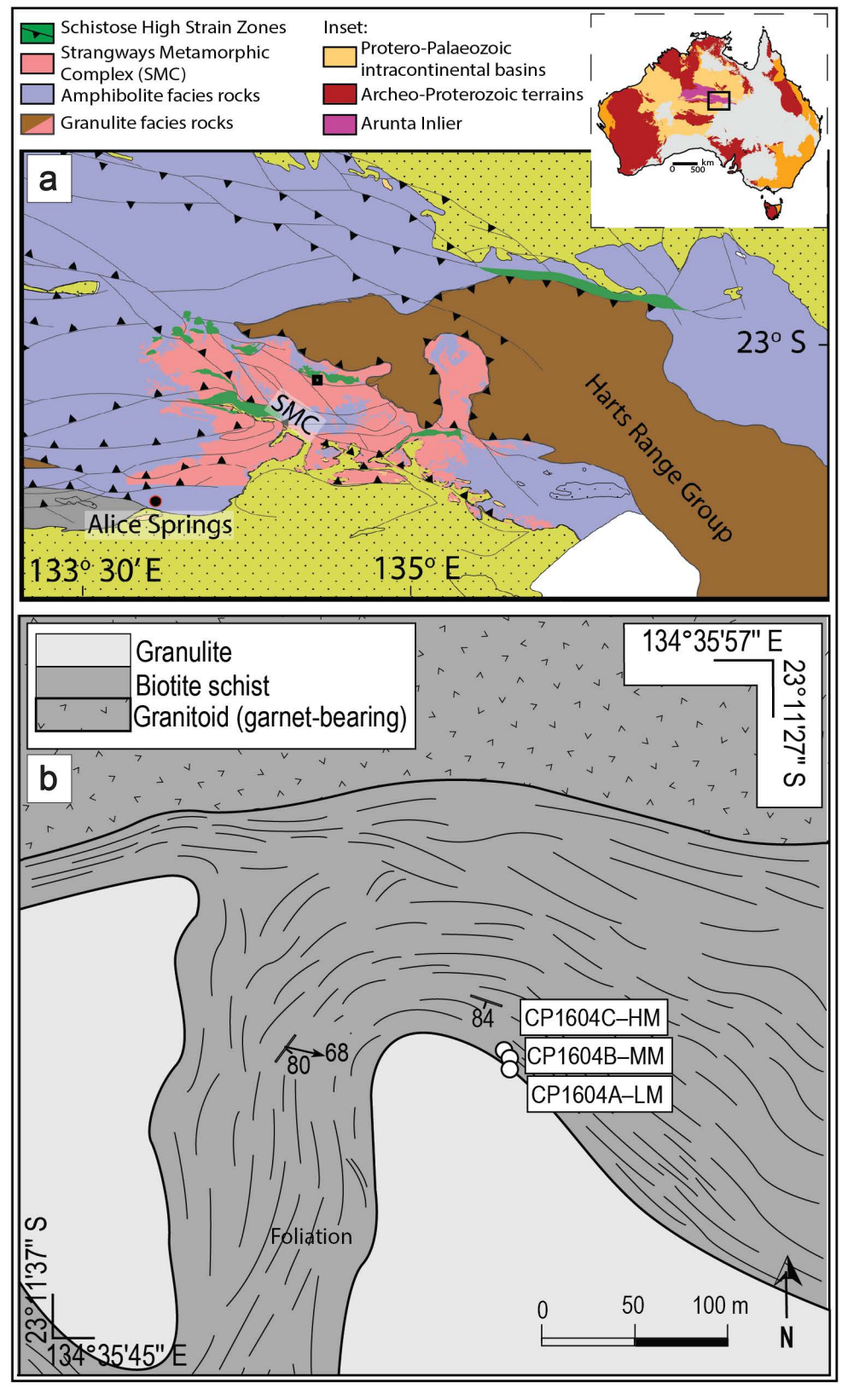
connected by a grain-boundary film (yellow arrow). (c) Interstitial ilmenite between garnet and biotite. (d) Synchysite and thorite inferred to have replaced monazite during melt–rock interaction. (e) Patches of synchysite (red arrow) within the shape of a precursor monazite grain (yellow arrow).

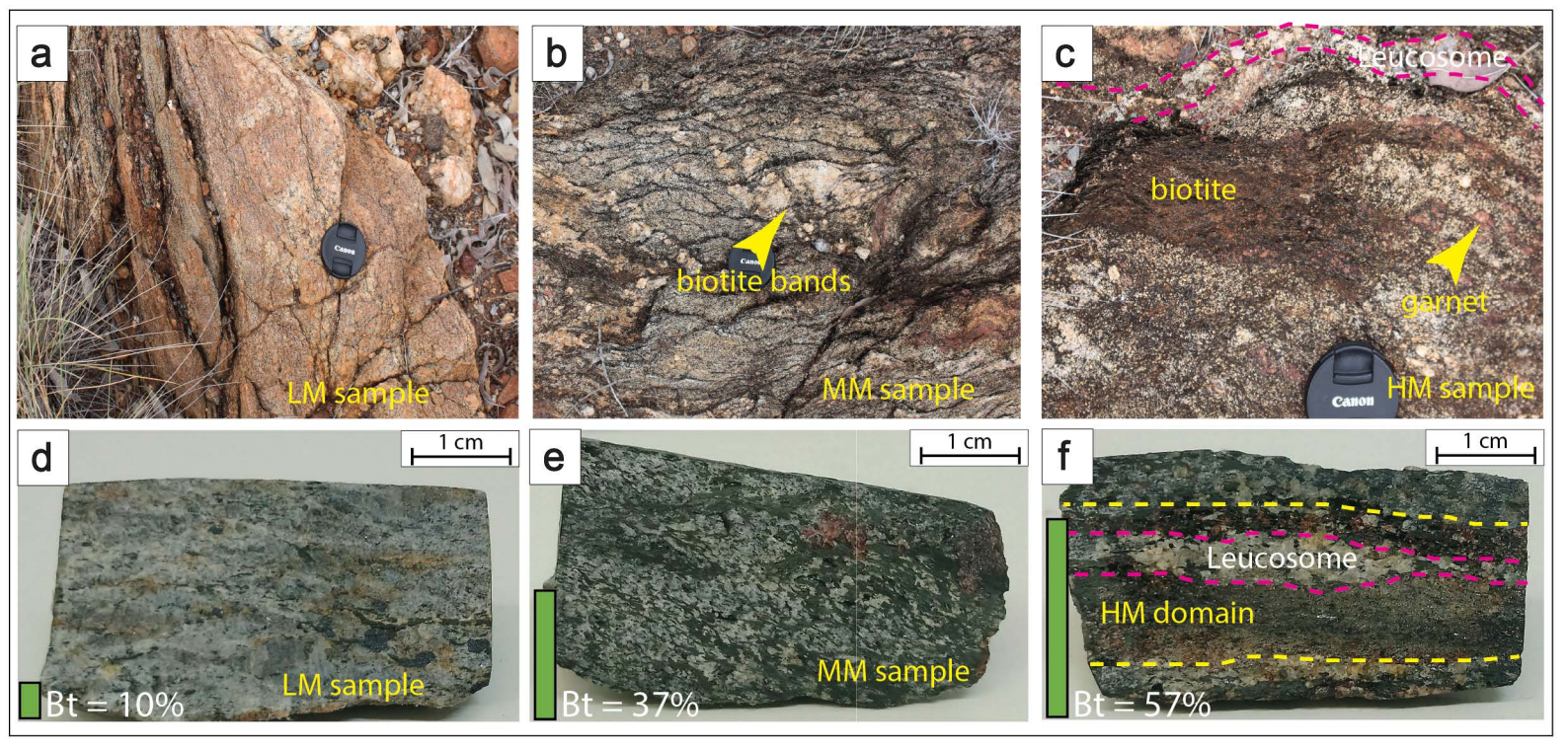
- **Figure 7.** Cathodoluminescence (CL) responses indicating open-system behaviour. (a–b) Adjacent plagioclase grains in MM sample CP1604B indistinguishable in BSE but showing contrasting CL (dark = blue arrow; bright = red arrows). Green arrow = CL texture in quartz. (c–d) Contact zone between HM domain and adjacent leucosome in sample CP1604C showing gradational CL response in quartz (red, blue, yellow arrows = progressively brighter CL domains separated by dashed lines; green arrow = late-stage features). (e–g) Contact zone of HM and leucosome domains in CP1604C showing plagioclase with contrasting CL, not visible in BSE. Grains with bright CL share orientation (black arrows; same green on Euler map). Red arrow = quartz bead; yellow arrow = quartz termination with low dihedral angle between plagioclase grains.
- **Figure 8.** EBSD orientation map of LM sample CP1604A. (a) Phase map of quartz and plagioclase (minor biotite). (b) Inverse pole figure (IPF) map of quartz showing highly variable orientations. (c) IPF map of plagioclase showing patches of similar orientation. (d) Subsets of similarly oriented plagioclase. (e) Pole figures showing clustered plagioclase orientations with some dispersion.
- **Figure 9.** EBSD analysis of garnet-bearing leucosome (quartz—plagioclase band) in sample CP1604C. (a) Phase map of quartz, plagioclase, and garnet (minor biotite). (b) Image and misorientation graph of a quartz grain relative to a reference point (white cross). (c) Euler map of neighbouring plagioclase grains; C-axis pole figure shows grains labelled 1 share identical orientation, likely connected in 3D. (d) Pole figures for plagioclase, quartz, and garnet.
- **Figure 10.** EBSD analysis of HM domain (biotite—garnet–ilmenite band) in sample CP1604C. (a) Phase map of biotite, garnet, ilmenite, apatite, and plagioclase. (b) Image and misorientation graph of ilmenite grain relative to reference point (white cross). (c) Euler map showing garnet with random orientation and low internal misorientation; rare garnet shows differently oriented core and rim (red arrow). (d) Pole figures for ilmenite, garnet, and biotite.
- **Figure 11.** Major-element mineral chemistry across the three samples. (a) Plagioclase ternary (An–Ab–Or). (b) Biotite ternary discrimination diagram (after Nachit *et al.*, 2005). (c) Ti *vs* XMg in biotite. (d) Ti *vs* XFe in biotite. (e) Garnet ternary (Py–Al+Sp–Gr). (f) CaO *vs* MnO (wt%) for garnet origin discrimination (after Harangi *et al.*, 2001).
- **Figure 12.** Rare earth element (REE) chemistry of minerals, normalised to primitive mantle (McDonough & Sun, 1995). (a) REE variation in biotite across all samples. (b) REE variation in garnet from MM and HM samples. (c) REE variation in plagioclase across all samples. (d) REE variation in plagioclase from HM sample relative to CL response.
- **Figure 13.** Conceptual model of shear zone initiation and widening. The first deformation cycle involves strain localisation due to stress or fluid-pressure buildup in precursor rocks (labelled A), triggering failure and melt ingress (Step 1). Syntectonic melt–rock interaction may both soften and harden the high strain shear zone (labelled B) until melt supply diminishes. Melt flux crystallises biotite and garnet, while also driving dissolution–precipitation hydration reactions within low-strain to static domains of the shear zone (labelled C). Subsequent melt pulses widen the shear zone by reactivating adjacent, partially hydrated, former low- to intermediate-strain zones through similar reactions, progressively softening and thickening the shear zone.

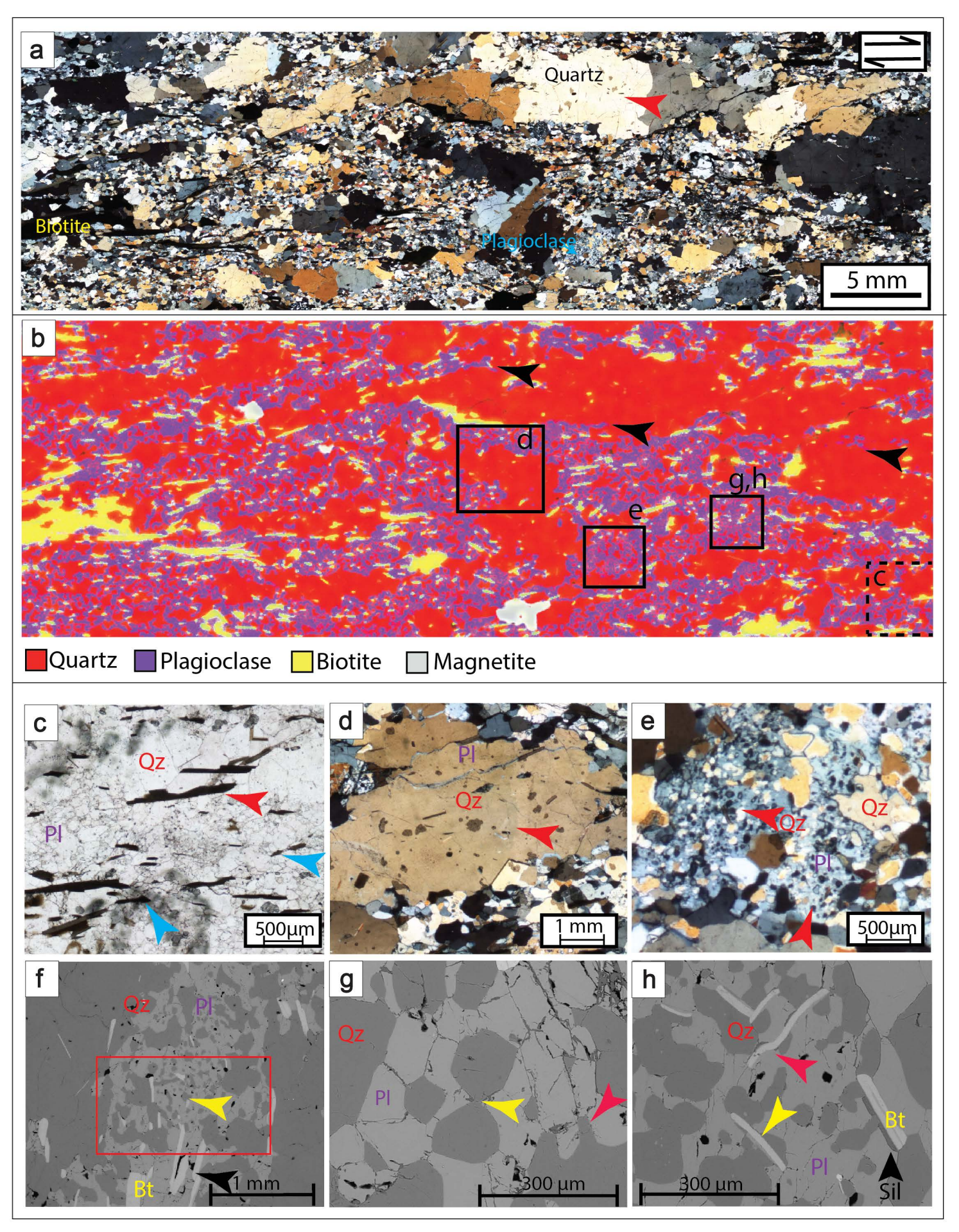
Supplemental data

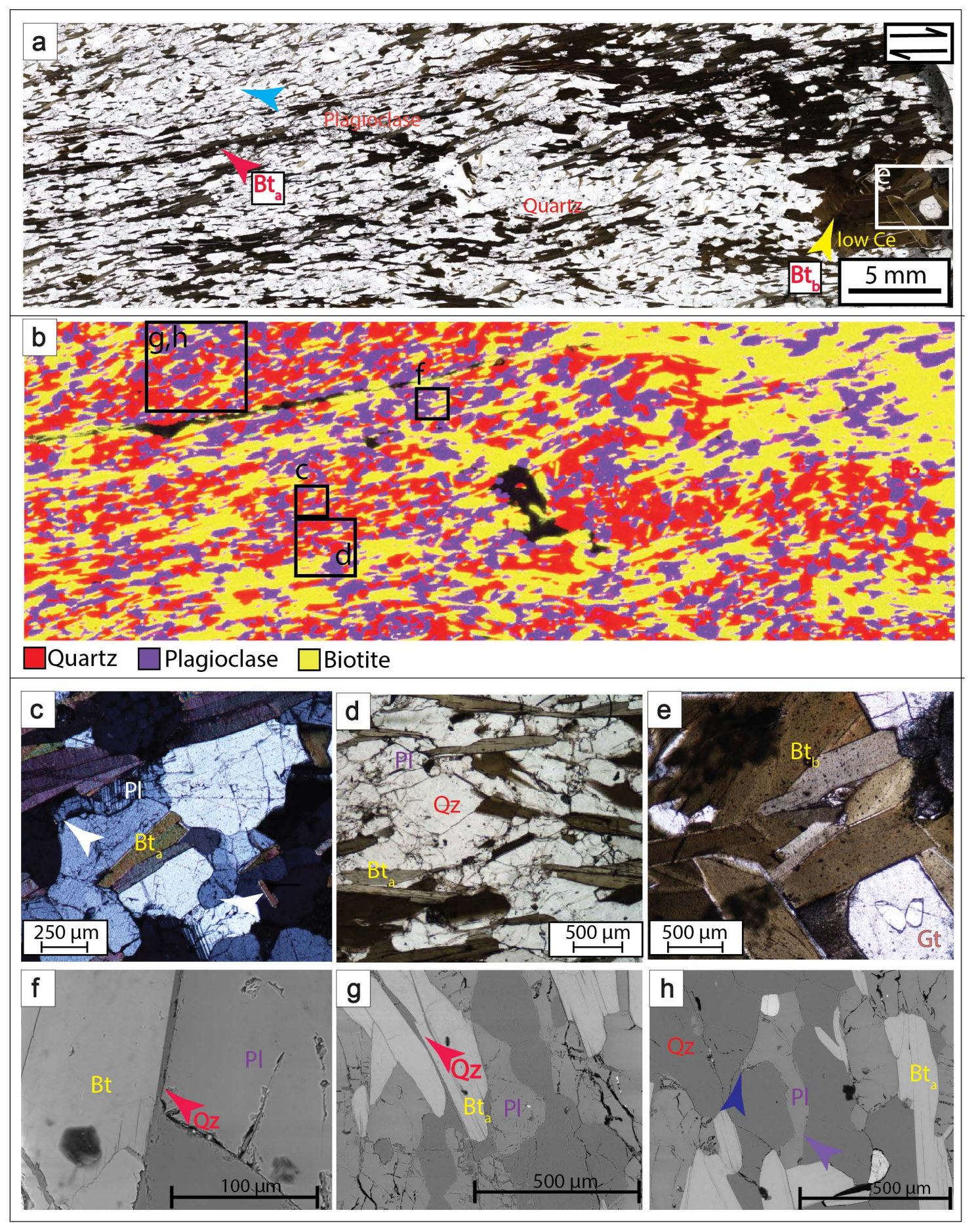
Tables S1-3. Electron microprobe data for biotite (S1), garnet (S2) and plagioclase (S3).

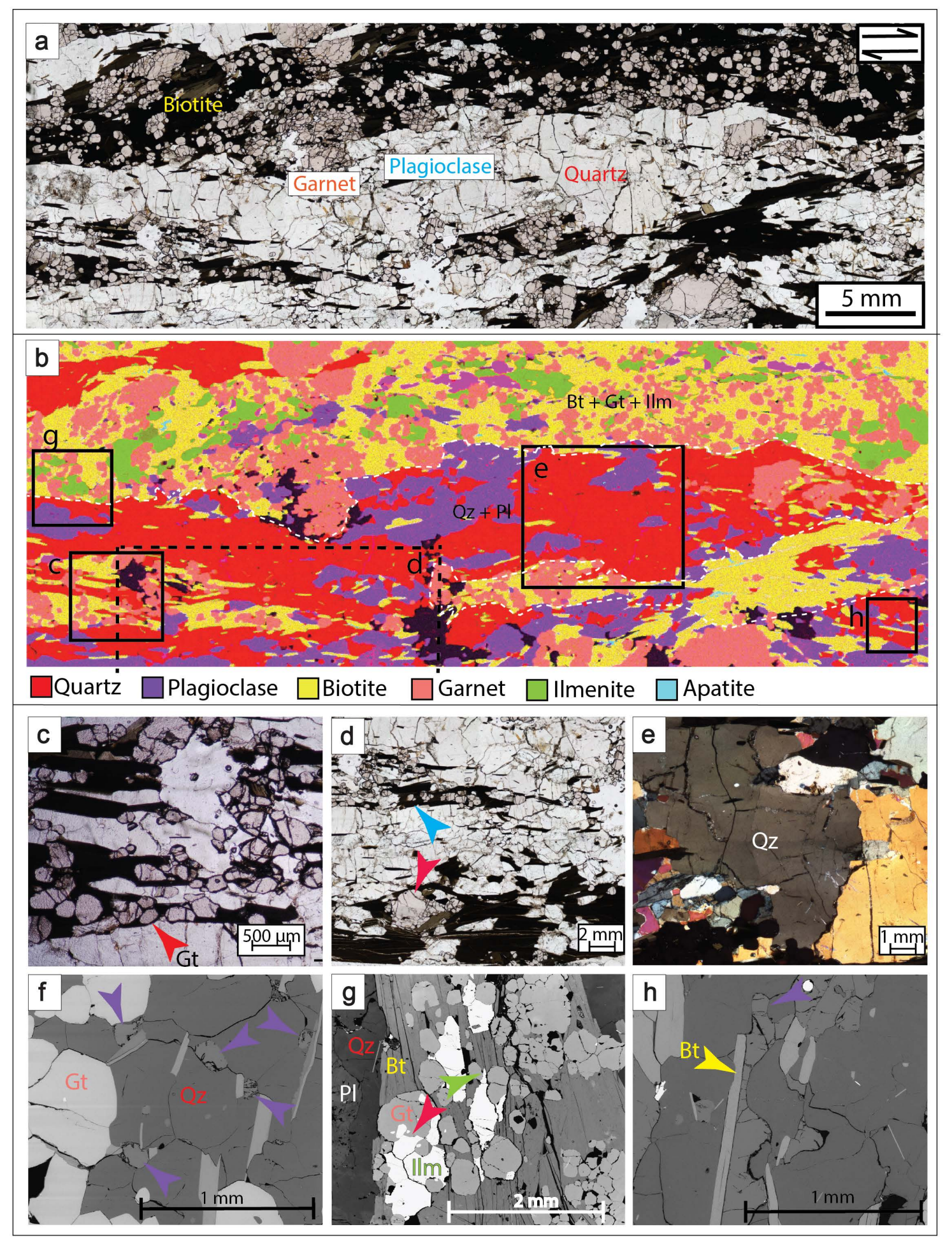
Tables S4-6. LA-ICP-MS data for plagioclase (S4), biotite (S5) and garnet (S6).

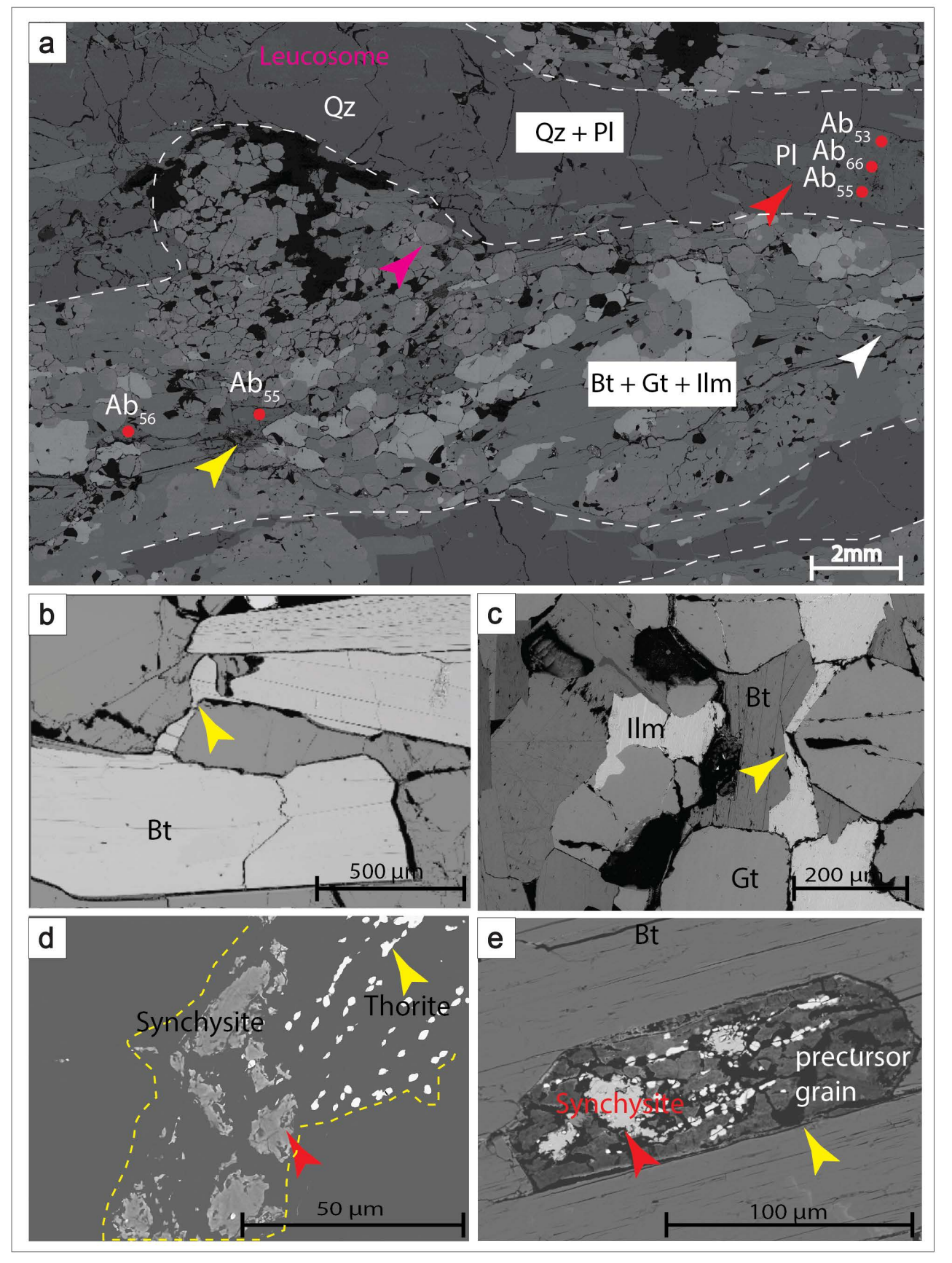


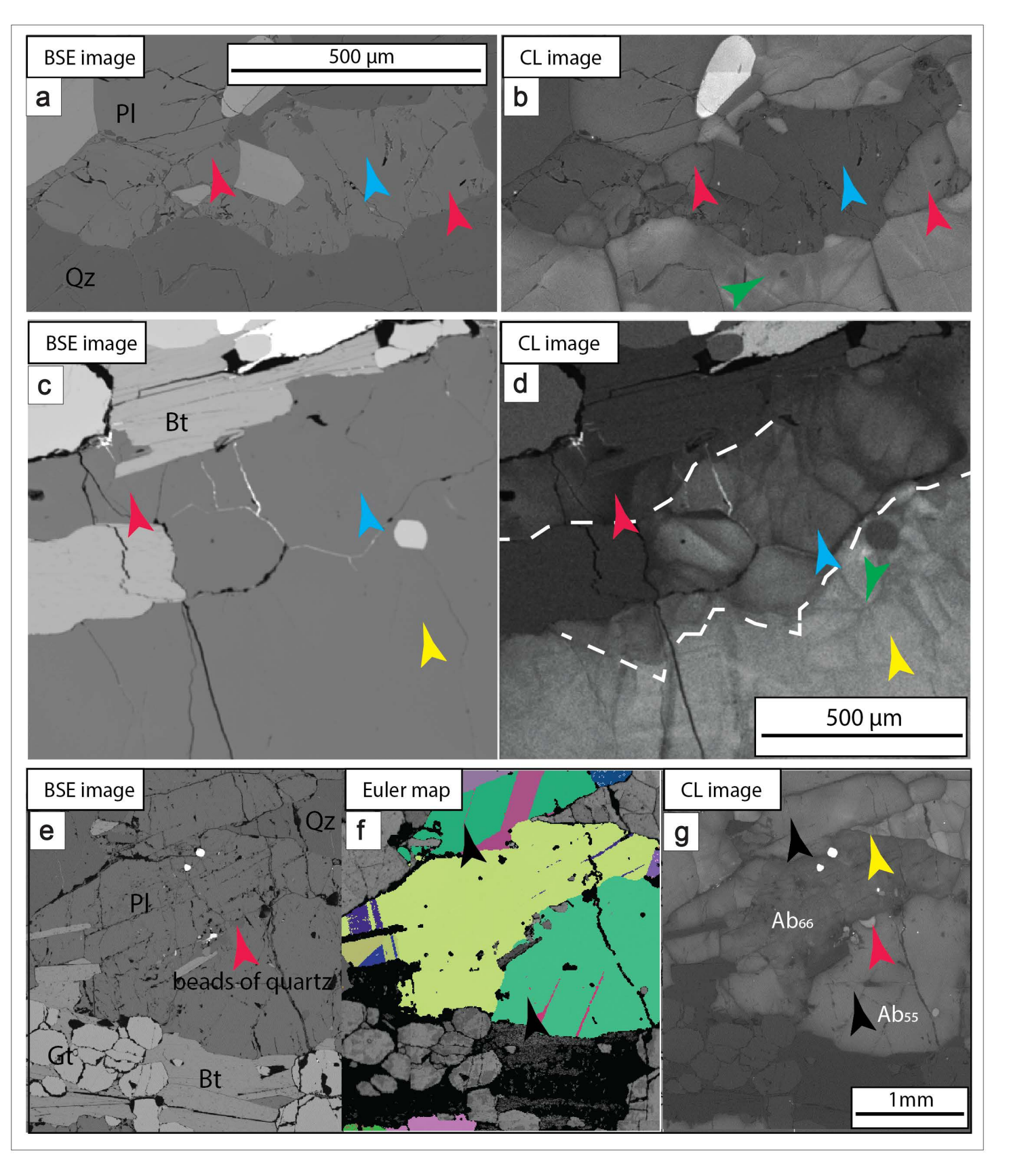


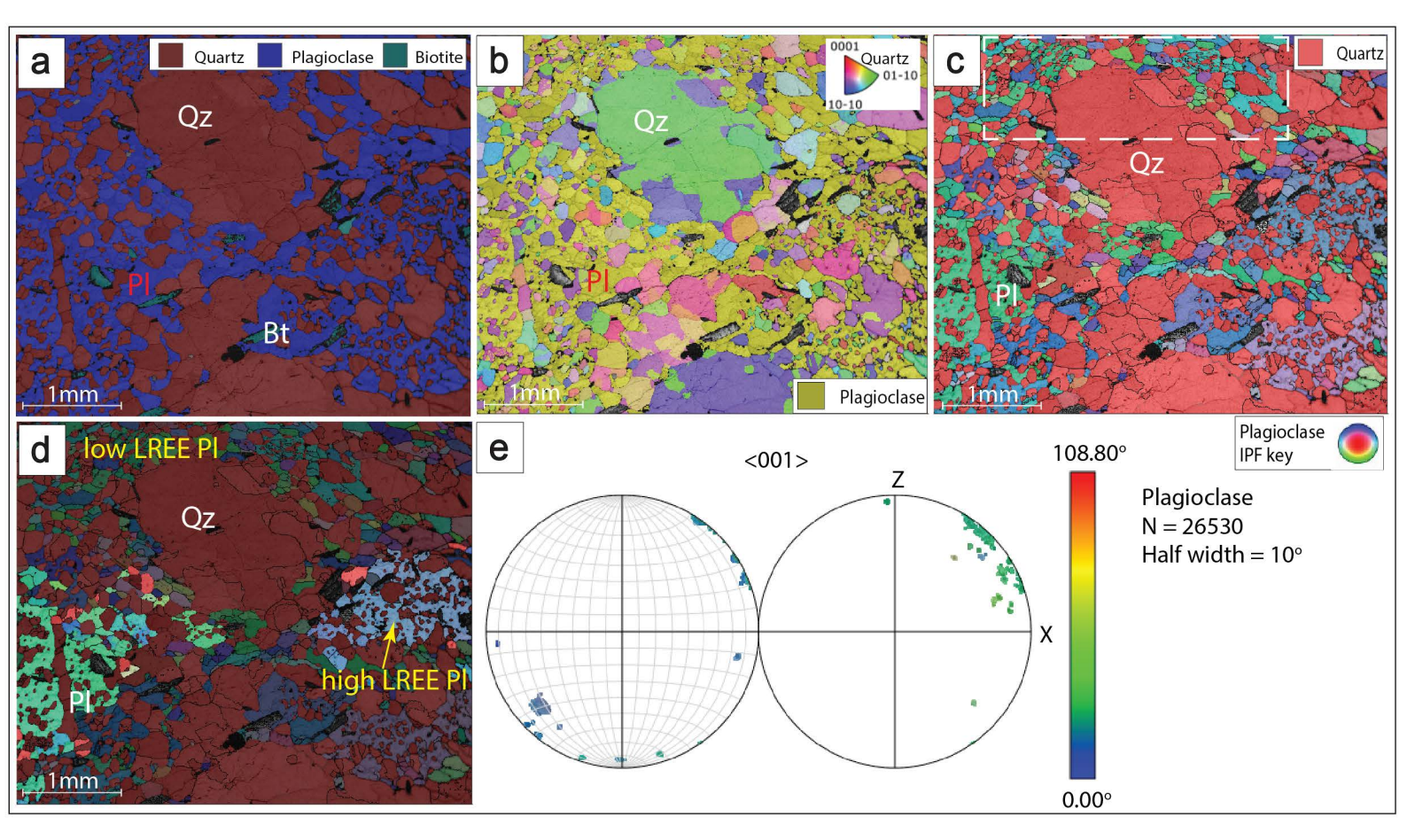


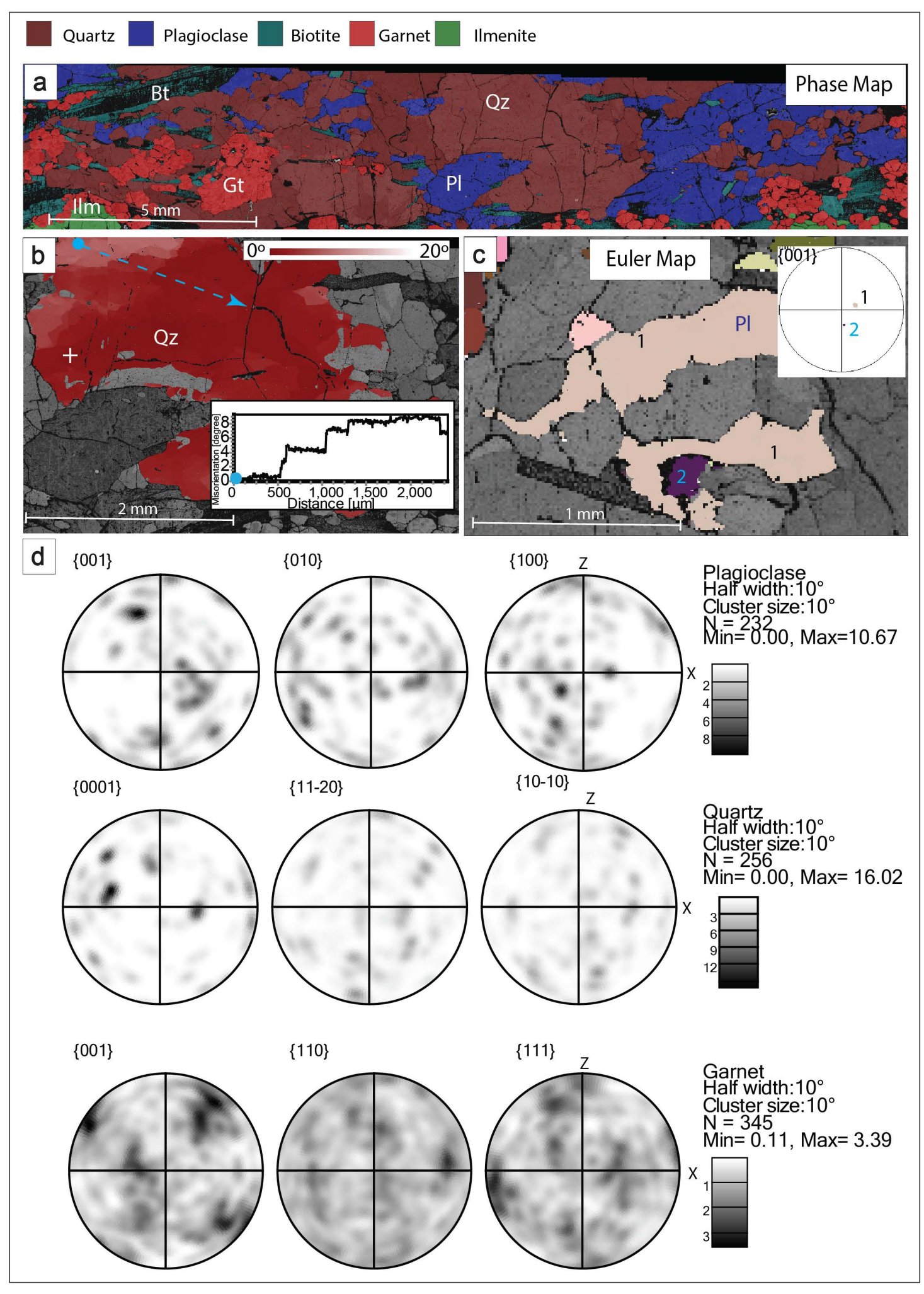


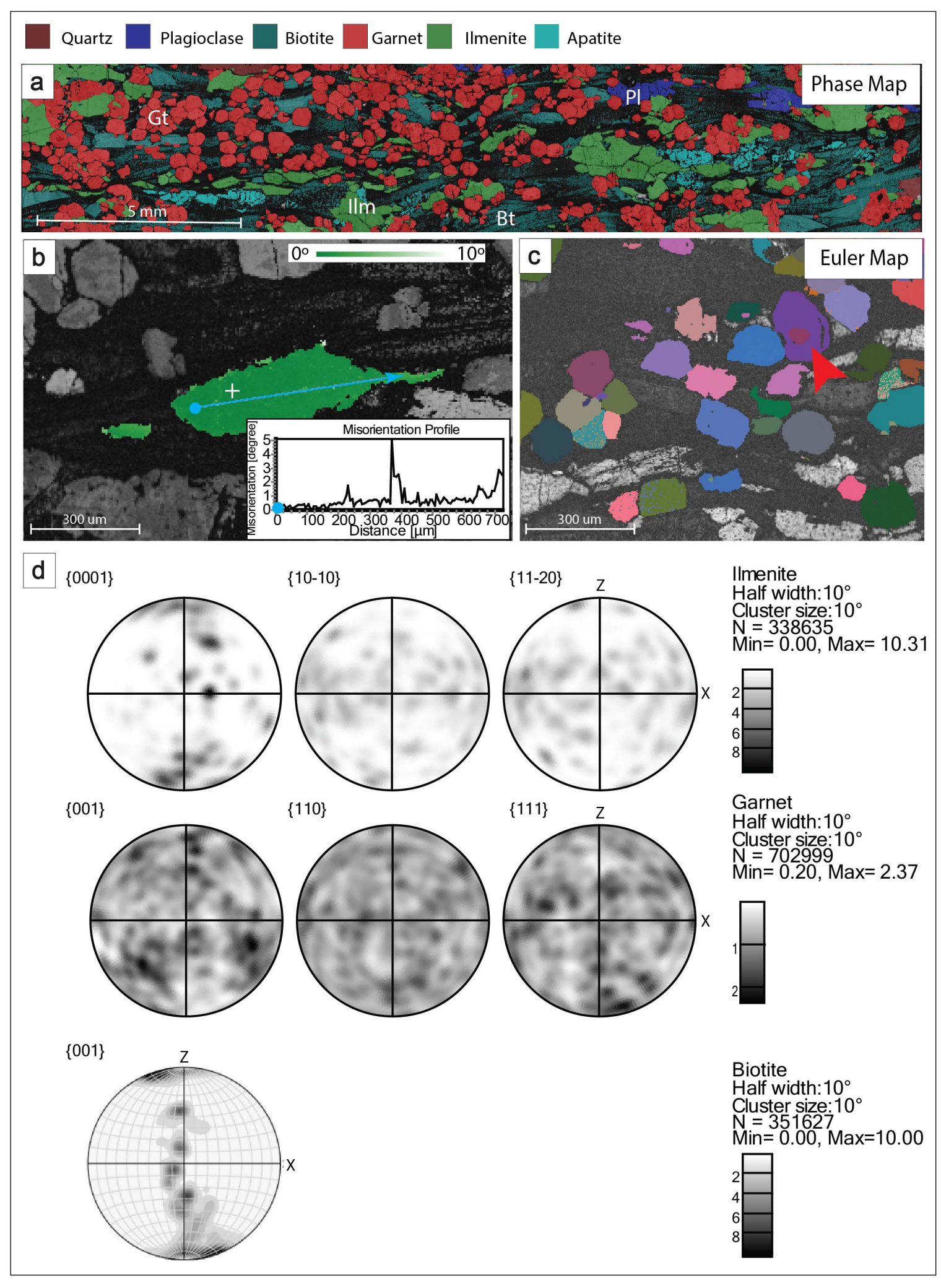


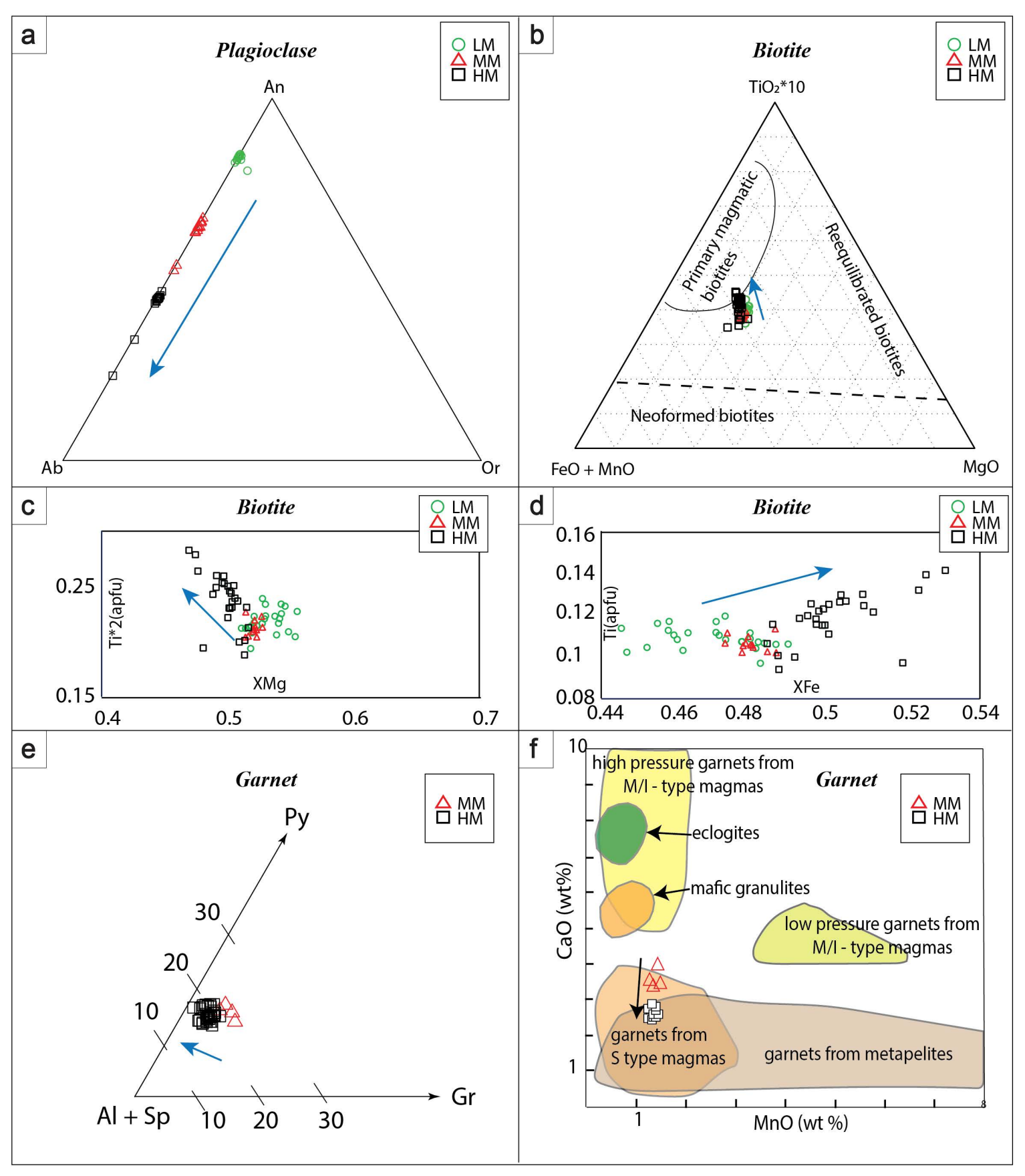


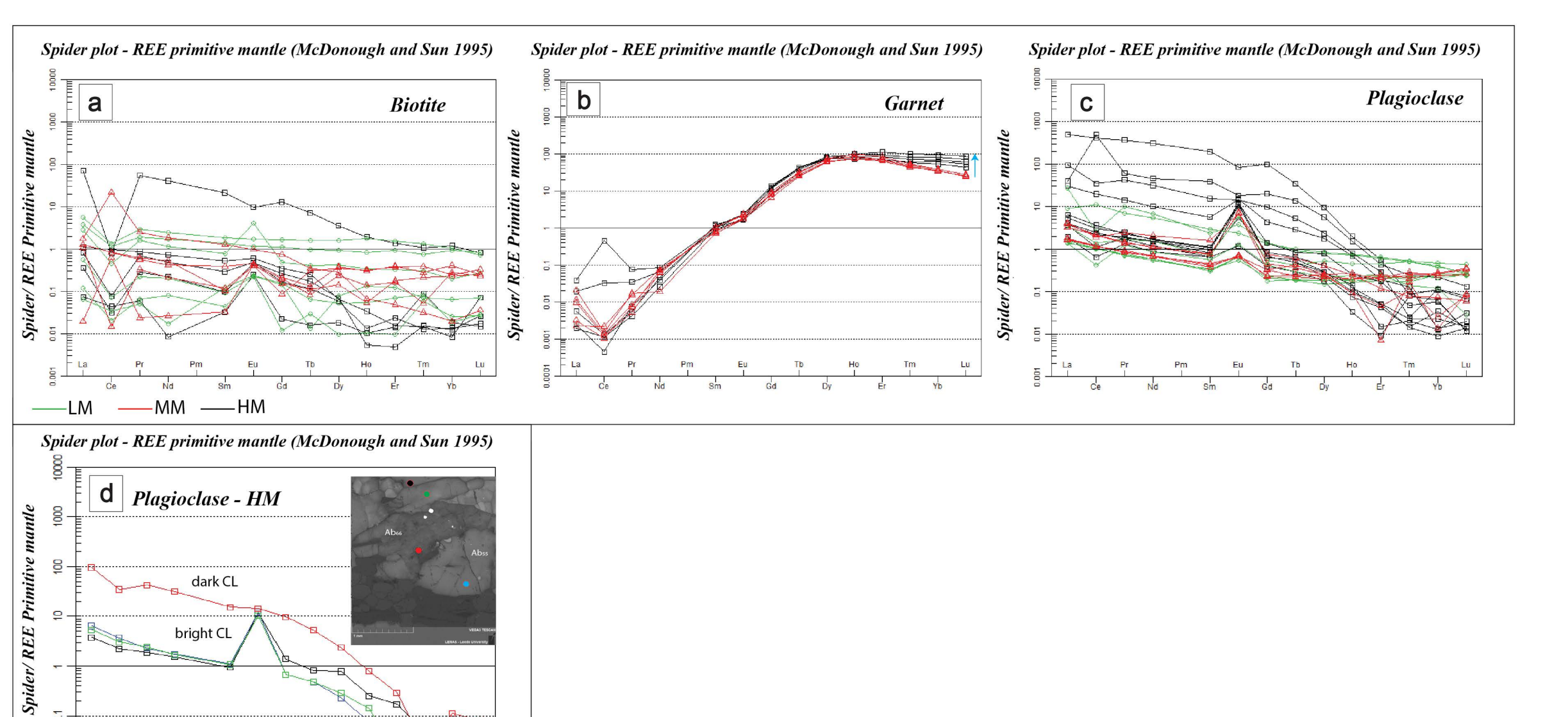


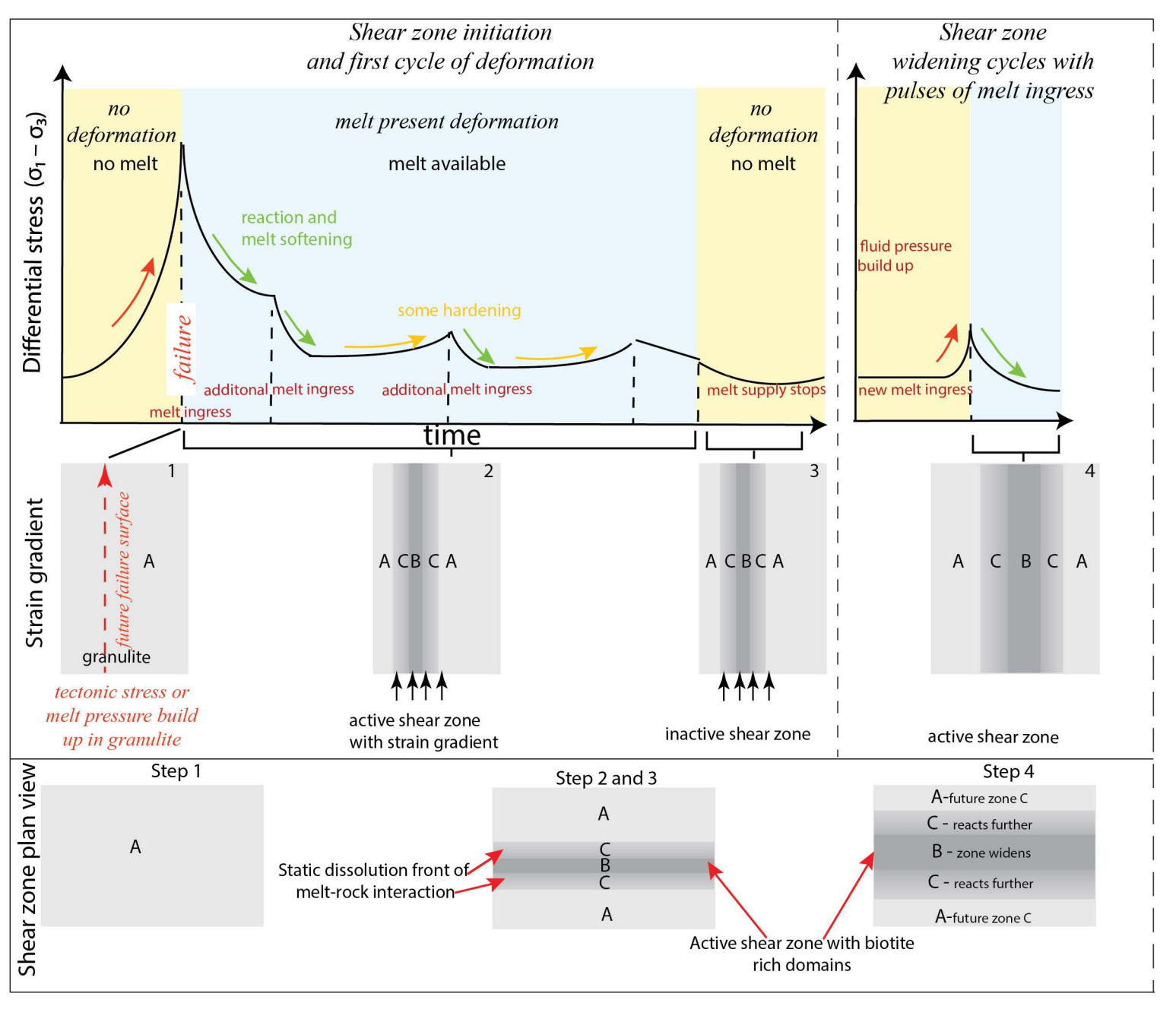












Sample	SiO ₂	TiO ₂	Al_2O_3	V2O3	Cr ₂ O ₃	FeO _t	NiO	MnO	MgO	CaO	Na ₂ O	K ₂ O	P ₂ O ₅	SO ₃	Cl	F	О	H_2O	Total
1604C_4	34.42	2.03	18.29	0.05	-	18.58	-	-	10.21	-	0.27	9.14	-	0.05	0.25	0.21	-	3.95	97.31
1604C_5	34.60	2.03	18.20	0.06	-	18.70	-	-	10.10	-	0.24	9.10	-	0.05	0.24	0.22	-	3.95	97.34
1604C_7	35.40	2.13	18.31	0.07	-	19.86	-	-	10.09	-	0.25	9.17	0.03	0.05	0.25	0.24	-	3.93	99.62
1604C_9	35.17	2.02	18.41	0.08	-	19.53	-	-	10.47	0.02	0.24	9.18	-	-	0.25	0.25	-	3.93	99.39
CP1604A_Bt1	32.67	1.70	17.67	0.06	-	18.46	-	0.05	11.54	0.23	0.15	6.28	-	0.35	0.27	0.19	-	4.01	93.49
CP1604A_Bt2	35.96	1.70	19.08	0.06	-	18.08	-	-	10.35	0.05	0.25	8.42	-	0.05	0.29	0.20	-	4.00	98.34
CP1604A_Bt3	35.75	1.96	17.97	0.05	-	18.21	-	-	11.26	-	0.31	9.11	0.03	0.03	0.27	0.27	-	3.96	99.01
CP1604A_Bt4	35.56	1.89	17.94	0.04	-	18.54	-	-	11.01	0.03	0.25	9.08	-	0.04	0.27	0.25	-	3.96	98.70
CP1604A_Bt5	35.38	1.95	18.09	0.08	-	18.50	-	0.05	11.10	-	0.31	8.90	-	-	0.28	0.26	-	3.96	98.69
CP1604A_Bt6	35.41	1.92	17.78	0.03	-	17.98	-	-	11.28	-	0.26	8.88	-	0.03	0.25	0.21	-	3.97	97.85
CP1604A_Bt7	34.91	1.97	17.96	-	0.04	18.14	-	0.06	11.41	0.14	0.27	8.26	-	-	0.25	0.21	-	3.98	97.45
CP1604A_Bt8	35.71	1.89	18.04	0.05	-	17.82	-	0.05	11.14	0.09	0.29	8.83	-	0.06	0.28	0.22	-	3.98	98.30
CP1604A_rim_Bt8	36.28	1.86	19.14	0.05	-	17.45	-	-	11.27	0.10	0.27	8.94	-	0.03	0.29	0.21	-	4.00	99.73
CP1604A_Bt9	35.60	2.05	17.95	0.05	-	18.59	-	0.07	11.15	-	0.27	9.01	-	0.06	0.26	0.23	-	3.96	99.09
CP1604A_Bt9_b	35.55	2.08	19.13	0.06	-	17.26	-	0.05	10.26	0.05	0.16	8.21	-	0.04	0.22	0.19	-	4.02	97.15
CP1604A_Bt10	35.68	1.92	18.23	0.07	0.04	19.19	-	-	11.11	-	0.30	9.12	-	0.03	0.32	0.22	-	3.95	100.01
CP1604A_Bt11	35.79	1.95	18.11	0.05	-	18.78	-	-	11.23	-	0.24	9.15	-	0.03	0.28	0.23	-	3.95	99.62
CP1604A_Bt12r	35.47	1.96	17.83	0.08	-	17.77	-	0.05	11.22	0.02	0.27	9.16	-	-	0.25	0.23	-	3.97	98.12
CP1604A_Bt12c	35.91	2.05	18.19	0.03	-	17.97	-	-	11.48	-	0.30	9.10	-	-	0.23	0.23	-	3.98	99.31
CP1604A_Bt13	35.31	1.79	17.40	0.02	-	19.21	-	0.06	11.31	0.07	0.21	8.45	-	-	0.28	0.20	-	3.96	98.13
CP1604A_Bt14	35.63	1.96	18.05	0.04	-	19.01	-	-	11.00	0.03	0.28	9.02	-	0.04	0.30	0.21	-	3.95	99.36
CP1604A_Bt15	36.00	2.07	18.14	0.05	-	18.20	-	-	11.48	-	0.31	9.11	-	0.03	0.30	0.21	-	3.97	99.71
CP1604A_Bt16	35.61	1.82	18.07	0.07	-	18.87	-	-	10.86	0.08	0.26	8.86	-	0.05	0.29	0.23	-	3.96	98.88
CP1604A_Bt17c	35.39	1.86	17.59	0.07	-	18.83	-	0.05	11.00	-	0.27	8.87	0.04	0.03	0.28	0.23	-	3.96	98.30
CP1604A_Bt17r	35.64	1.88	17.81	0.03	-	18.85	-	-	11.01	-	0.26	8.90	-	0.04	0.30	0.23	-	3.96	98.74
CP1604A_Bt18	35.11	1.83	17.59	0.07	-	19.10	-	0.06	10.62	0.07	0.22	8.68	-	0.03	0.28	0.21	-	3.95	97.68
CP1604A_Bt19c	35.74	1.87	18.07	0.03	-	18.97	-	-	10.82	-	0.29	8.92	-	0.03	0.35	0.23	-	3.95	99.09
CP1604A_Bt19r	35.24	1.84	18.15	0.04	0.04	19.10	0.05	-	10.76	0.10	0.23	8.29	-	0.04	0.28	0.22	-	3.96	98.18
CP1604A_Bt20	35.65	1.86	17.65	0.05	-	18.98	-	0.05	10.89	0.09	0.21	8.42	-	0.04	0.27	0.24	-	3.97	98.19
CP1604B_Bt1	36.44	1.98	18.01	0.09	0.08	18.93	-	-	11.22	0.03	0.21	8.98	-	-	0.24	0.23	-	3.96	100.26
CP1604B_Bt2	35.62	1.92	17.82	0.09	0.07	19.13	-	-	11.09	0.03	0.33	8.97	-	0.04	0.22	0.23	-	3.95	99.37
CP1604B_Bt3	35.49	1.99	17.93	0.09	0.10	19.46	-	-	10.97	-	0.23	9.26	-	0.06	0.28	0.21	-	3.94	99.86
CP1604B_Bt4	35.76	1.87	17.96	0.09	0.09	18.65	-	-	11.09	-	0.29	9.12	-	-	0.29	0.26	-	3.95	99.24
CP1604B_Bt5	35.77	1.79	17.70	0.07	0.10	19.00	-	-	11.09	0.02	0.28	9.05	0.03	0.05	0.27	0.20	-	3.95	99.24
CP1604B_Bt6	35.71	1.85	17.77	0.08	0.11	19.02	-	0.04	10.98	-	0.26	9.22	-	-	0.32	0.19	-	3.95	99.35
CP1604B_Bt7	35.68	1.85	17.90	0.09	0.09	18.91	-	-	11.02	0.02	0.27	9.10	-	-	0.28	0.22	-	3.95	99.22
CP1604B_Bt8	35.79	1.84	18.13	0.08	0.11	18.95	-	0.06	10.93	0.03	0.30	9.04	-	0.04	0.27	0.23	-	3.95	99.60
CP1604B_Bt9	35.57	1.79	18.08	0.08	0.11	18.85	-	0.04	10.72	0.03	0.26	9.01	-	-	0.28	0.22	-	3.95	98.83
CP1604B_Bt10	35.49	1.87	18.08	0.08	0.12	19.19	-	-	11.16	-	0.30	9.25	-	0.05	0.33	0.22	-	3.94	99.90
CP1604B_Bt11	35.42	1.85	18.06	0.11	0.15	19.02	-	-	11.01	-	0.29	9.41	-	0.05	0.27	0.23	-	3.94	99.65
CP1604B_Bt12	36.44	1.78	17.29	0.08	0.07	18.98	-	-	10.68	0.09	0.21	8.66	0.03	0.03	0.26	0.22	-	3.97	98.64
CP1604C_Bt33	34.86	2.15	18.21	0.04	0.07	19.27	-	-	9.89	-	0.32	9.43	-	-	0.22	0.15	-	3.94	98.43
CP1604C_Bt31	35.37	2.22	18.35	0.05	-	19.48	-	-	10.19	-	0.23	9.24	-	-	0.24	0.22	-	3.94	99.40

Table S1 - Microprobe major element data for biotite

Sample	SiO_2	TiO_2	Al_2O_3	V2O3	Cr_2O_3	FeO_t	NiO	MnO	MgO	CaO	Na ₂ O	K_2O	P_2O_5	SO_3	Cl	F	О	H_2O	Total
CP1604C_Gt1	36.61	-	21.03	-	-	33.35	-	1.22	3.92	2.90	-	-	-	-	-	-	0.03	0.00	99.07
CP1604C_Gt2	36.58	-	21.08	-	-	33.31	-	1.19	3.98	2.85	-	-	-	-	-	-	0.03	0.00	99.02
CP1604C_Gt3	36.54	-	21.16	-	0.06	33.97	-	1.24	3.43	2.72	-	-	-	-	-	-	0.02	0.00	99.14
CP1604C_Gt6	36.56	-	20.85	-	-	33.61	-	1.17	3.66	2.83	-	-	-	-	-	-	0.03	0.00	98.70
CP1604C_Gt8	36.82	-	21.04	-	-	33.62	-	1.27	3.65	2.99	-	-	0.04	-	-	-	0.02	0.00	99.44
CP1604C_Gt40	37.30	-	21.62	-	-	33.72	-	1.24	4.07	2.95	-	-	-	-	-	-	0.01	0.00	100.92
CP1604C_Gt41	37.32	-	21.59	-	-	34.00	-	1.24	3.94	2.99	-	0.01	-	-	-	-	0.01	0.00	101.10
CP1604C_Gt42	37.14	-	21.21	-	-	34.10	-	1.21	3.97	3.05	-	-	-	-	-	-	0.02	0.00	100.69
CP1604C_Gt43	36.60	-	21.12	-	-	33.81	-	1.20	3.88	2.88	-	-	-	-	-	-	0.00	0.00	99.49
CP1604C_Gt44	36.79	-	21.26	-	-	34.57	-	1.20	3.75	2.87	0.03	-	-	-	-	-	0.01	0.00	100.47
CP1604C_Gt45	36.85	-	21.06	-	0.05	34.73	-	1.27	3.18	2.88	-	-	-	-	-	-	0.02	0.00	100.05
CP1604B_Gt1	37.42	-	21.55	-	-	33.15	-	1.21	3.38	3.99	-	-	-	-	-	-	0.00	0.00	100.71
CP1604B_Gt2	37.18	-	21.31	0.03	-	32.97	-	1.10	4.02	3.66	-	-	-	-	-	-	0.02	0.00	100.28
CP1604B_Gt3	37.20	-	21.11	-	-	32.76	-	1.23	3.77	3.55	-	-	-	-	-	-	0.02	0.00	99.63
CP1604B_Gt4	37.04	-	21.01	-	0.05	33.30	-	1.18	3.76	3.54	-	-	-	-	-	-	0.01	0.00	99.88
CP1604C_Gt71	36.40	-	20.86	-	-	33.56	-	1.22	3.78	2.79	0.05	-	-	-	-	-	0.02	0.00	98.67
CP1604C_Gt72	36.83	-	20.68	-	-	33.57	-	1.22	3.71	2.78	-	-	-	-	-	-	0.03	0.00	98.82
CP1604C Gt73	36.68	-	21.03	-	-	34.30	-	1.22	3.33	2.81	-	-	-	-	-	-	0.02	0.00	99.39
CP1604C_Gt85	36.63	-	21.06	-	-	34.06	-	1.23	3.29	2.82	-	-	-	-	-	-	0.03	0.00	99.12
CP1604C Gt76	36.95	-	21.07	0.05	-	33.82	-	1.24	3.60	2.90	-	-	0.03	-	-	-	0.02	0.00	99.67
CP1604C Gt87	36.99	_	21.33	-	-	34.39	_	1.29	3.78	2.89	-	-	-	-	-	-	0.01	0.00	100.69
CP1604C Gt77	36.90	-	20.96	-	-	33.87	-	1.17	3.60	2.87	-	-	-	-	-	-	0.00	0.00	99.38
CP1604C Gt78	36.55	_	20.87	-	-	33.66	_	1.31	3.43	2.91	0.04	_	-	_	-	-	0.03	0.00	98.79
CP1604C Gt86	36.56	-	20.73	-	-	33.56	-	1.17	3.54	2.72	-	-	-	-	-	-	0.03	0.00	98.31
CP1604C_Gt74	37.13	_	20.91	-	-	34.20	_	1.23	3.63	2.71	-	_	-	_	-	-	0.03	0.00	99.85
CP1604C Gt75	36.66	_	20.94	-	-	34.54	_	1.31	3.16	2.88	-	_	-	_	-	-	0.03	0.00	99.52
CP1604C Gt89	36.50	_	20.85	-	-	34.56	_	1.20	3.28	2.69	-	_	-	_	-	-	0.03	0.00	99.10
CP1604C Gt88	36.78	_	21.33	_	-	33.57	_	1.15	3.75	2.90	_	_	_	_	-	_	0.01	0.00	99.56
CP1604C Gt88r	36.92	_	20.93	_	-	34.08	_	1.24	3.52	2.83	_	_	_	_	-	_	0.01	0.00	99.52
CP1604C_Gt78r	36.94	_	20.87	-	-	34.10	_	1.27	3.53	2.68	-	-	0.03	-	-	-	0.02	0.00	99.44
CP1604C Gt79r	36.81	_	20.78	-	-	34.85	_	1.27	3.29	2.70	-	_	0.05	_	-	-	0.01	0.00	99.78
CP1604C_Gt81r	36.93	_	20.82	-	-	34.30	0.06	1.27	3.40	2.86	-	_	-	_	-	-	0.01	0.00	99.65
CP1604C Gt81brr	36.72	_	21.03	-	-	34.26	_	1.17	3.42	2.78	-	_	-	_	-	-	0.02	0.00	99.40
CP1604C Gt80	36.77	_	20.88	_	-	34.56	_	1.33	3.22	2.88	_	_	_	_	-	_	0.01	0.00	99.65
CP1604C Gt82	36.74	_	20.82	-	-	33.92	_	1.19	3.55	2.67	-	_	-	_	-	-	0.03	0.00	98.91
CP1604C Gt94	36.78	_	20.56	-	-	34.07	_	1.31	3.54	2.76	-	_	-	_	-	-	0.03	0.00	99.05
CP1604C Gt83	36.85	_	21.09	_	-	34.28	_	1.26	3.24		0.04	_	0.03	_	-	-	0.00	0.00	99.82
CP1604C Gt84c	36.85	_	21.30	0.02	_	33.72	_	1.27	3.90	2.97	_	_	_	_	_	_	0.03	0.00	100.06
CP1604C_Gt84r	36.38	_	20.83	-	_	33.63	_	1.27		2.91	_	0.02	_	_	_	_	0.04	0.00	98.35
CP1604C Gt75a	36.56	_	20.59	0.02	_	33.92	_	1.20	3.14	2.68	0.04	-	_	_	_	_	0.04	0.00	98.19
CP1604C Gt75b	36.94	_	20.62	-	_	33.57		1.16	3.60	2.92	-	_	_	_	_	_	0.03	0.00	98.83
CP1604C Gt75c	36.56	_	20.95	0.03	_	33.82	_	1.32	3.58		_	_	_	_	_	_	0.04	0.00	99.06
CP1604C Gt75d	36.54	_	20.92	-	_	33.93			3.38		_	_	0.03	_	_	_	0.03	0.00	98.94
									2.50										

 $\textbf{Table S2} \text{ -} \ \text{Microprobe major element data for garnet}$

Total	98.15557	98.54541	99.34784	98.83583	98.95997	99.30817	98.57584	62609.66	99.57039	99.54531	99.45216	99.61597	98.73435	99.43615	99.27609	94.02961	99.27641	98.90211	98.69839	99.54532	98.4725	99.25561	98.54615	99.27258	97.16846	98.9938	98.73414	98.46487	98.88141	99.33571	99.51099	99.33692	99.14589	98.87245	98.99513	99.59376	98.68479	98.19423	98.73265	97.91689	99.00078	98.47502	98.74857	99.43067	99.05863	98.70459	97.36305	97.95288
H20	0	0	0	0	0	0	0	0	0	0	0	0	0	0	0	0	0	0	0	0	0	0	0	0	0	0	0	0	0	0	0	0	0	0	0	0	0	0	0	0	0	0	0	0	0	0	0	0
0	0.010098	0.01149	0.000446	0.00206	-0.00257	0.006134	0.005909	0.007744	0.012089	0.006275	0.004902	0.008064	0.005661	0.00779	0.004097	-0.02114	0.003178	0.011765	0.003799	0.005447	-0.00716	0.014687	0.003578	0.002434	0.00359	0.010349	-0.00291	0.016792	-0.00493	-0.00614	0.007946	0.002766	0.009819	0.003384	-0.00043	0.006729	0.001614	0.01009	-0.00013	0.023541	0.000237	0.00333	-0.01165	0.00066	0.008438	-0.00558	0.006226	0.016247
ш	-	,	,	,		-	-	,	,	,	,	,	,	1	,		,	,	,	,		,	-	,	,	,		-			-	,	-	,		,	,			-	-	,			-		,	,
Ö	0.018383	0.020025		,		,			,		,	,	,		,	0.094553		,		,	,	,	,	,	0.019041			1	,		,									,				0.025081				,
803		1		,		0.03606	1	1	,	1	0.026713	1	,		,	0.028214	1	,	1	,	,	0.025504	,	,	,		1	1	,		,							,	1	,	1	1	1				0.025719	
P205		,										,	,	0.031137		0.046965	0.030875	,	0.023742		0.027088		0.023273		0.025919										0.050291		0.030294			,					0.035528	0.099852		0.067486
K20	0.039113	0.069868	0.08115	0.058487	0.013506	0.04	0.099239	0.030759	0.014177	,	0.171873	0.026477	0.012633			0.52187	0.023715	,		0.038936	0.101285	0.038134	0.028076	0.067705	0.095458	0.028003	0.023098	0.037686	0.023807	0.040088		0.033565	0.056376	0.017646	0.038596	,	0.044196	0.08814	0.085391	0.062674	0.059559	0.039624	0.072578	0.053735	0.060415	0.050707	0.06453	0.039885
Na2O	8.56432	6.13683	6.137	6.14673	1.68821	1.85607	1.66995	1.72867	1.81074	1.83323	1.76833	1.88907	1.8834	1.99667	1.96362	1.34488	1.89871	1.69497	1.7721	4.18177	3.84641	3.80682	3.77005	3.99585	3.62087	3.97641	4.21045	3.97124	3.76793	4.1397	3.9881	3.83877	3.92405	4.13986	5.17705	3.71011	5.2876	6.08463	6.02541	6.07749	6.14111	6.24837	6.36408	6.4819	6.15485	5.97411	7.25528	6.17357
CaO	4.75623	9.21895	9.11432	9.10995	16.9284	16.5039	16.5691	16.6972	16.9369	16.8103	16.7508	16.829	16.805	16.8048	16.5562	12.2358	16.8357	16.652	16.8565	12.9305	12.8301	13.2133	13.2902	12.6932	12.0492	12.9676	13.0865	12.9677	13.2558	12.7881	13.162	13.3234	13.1261	12.7642	10.997	13.5999	10.5995	9.11797	9.22495	8.92358	9.0733	9.00018	9.06226	9.03329	9.13161	9.5379	6.6127	9:000:6
MgO	0.026727	0.028747				0.023709	0.026455	,		,		,	,			0.220916	,	,	1	,	,		,	0.03353	0.08141										0.022924		0.02138	,	1	,		1					0.024299	,
MnO		,	,	,		,		0.03792	,		,	,	,	,		,		,	,	,	,	,	,		,	,	,	,	,		,	,	,	,	·			,		,	,	,	,		,	,	í	
OiN		,	,	,	,	,		,	,		,		,	,		,		,	,	,	,	,	,		,	,	,	,	,		,	,	,		·		0.04715			,	,	,	,	,	,	,	,	
FeOt		,	0.049923		0.076826	1	0.073889	0.046696	0.041784	0.0464	0.088645	,	0.047355	0.050057	0.056432	0.28365	0.106528	0.087474	0.0629	0.092367	0.110873	0.07226	0.088169	0.065756	0.10727	0.078336		0.052348	990.0	0.054441	0.068442	0.126422	0.059549	0.07496			0.043054 0	,	0.042831	,	0.048577	0.131217	ı	0.147404	0.097384			
Cr203				,		,			,		,		,	1	,	,				,	,	,	,	,	,		,	,	,	1	,		,		,			,		,	,		,		,	1	·	
V2O3 (,					1	,		,		0.022561	,		0.030343		,	,	0.025352	,	,		,		,				,					1		,		,	1	,		,						0.021832
AI203	23.6618	27.623	27.7876	27.4328	34.2146	34.3864	33.7621	34.4733	34.5921	34.4297	34.2266	34.3926	34.0987	34.1053	33.978	34.5152	34.348	34.1912	33.8944	30.6605	30.5258	31.1343	31.0924	30.6483	31.0252	30.647	30.4921	30.5282	30.8716	30.8404	31.1278	31.1143	30.8643	30.7551	28.9238	31.6573	28.7806	27.1883	27.5063	27.1339	27.3797	27.2024	27.3826	27.3425	27.3929	27.714	25.0461	27.1363
Ti02		,		,		,			,		,		,			,		,	,	,		,					,	,	,	0.026218	,									,	,	,	,					
SiO2	61.0789	55.4365	56.1774	56.0858	46.041	46.4559	46.3692	46.5875	46.1626	46.4194	46.4143	46.4482	45.8816	46.4404	46.6874	44.7587	46.0297	46.2647	46.0596	51.6358	51.0381	50.9506	50.2504	51.7658	50.1405	51.2861	50.9249	50.8909	50.9012		51.1567	50.8977	51.1057	51.1173	53.7859	50.5529	53.8294	55.7051	55.8479	55.6957	56.2983	55.8499	55.8787	56.3461	56.1775	55.3336	58.3282	55.4912
Sample	1604C_11	1604C_12	1604C_13	1604C_14	CP1604A_Plg43	CP1604A_Plg44	CP1604A_Plg42	CP1604A_Plg45	CP1604A_Plg46	CP1604A_Plg47	CP1604A_Plg48	CP1604A_Plg49	CP1604A_Plg50	CP1604A_Plg51	CP1604A_Plg52	CP1604A_Plg53	CP1604A_Plg54	CP1604A_Plg55	CP1604A_Plg56	CP1604B_PI1	CP1604B_PI1r	CP1604B_Pl2c	CP1604B_Pl2r	CP1604B_Pl3c	CP1604B_Pl3r	CP1604B_Pl4	CP1604B_PI5	CP1604B_PI6	CP1604B_PI7	CP1604B_PI8	CP1604B_PI9	CP1604B_PI10	CP1604B_PI11	CP1604B_PI12	CP1604B_PI13	CP1604B_PI14	CP1604B_PI15	CP1604C_Plg63	CP1604C_Pl65	CP1604C_Pl64	CP1604C_Plag66	CP1604C_Plg68	CP1604C_Plg67c	CP1604C_Plg67r	CP1604C_Plg69	CP1604C_Plg70ar	CP1604C_Plg70c	CP1604C_Plg70br

Table S3 - Microprobe major element data for plagioclase

Element	La139	Ce140	Pr141	Nd146	Sm147	Eu153	Gd157	Tb159	Dy163	Ho165	Er166	Tm169	Yb172	Lu175
610	446.52	459.54	454.23	436.24	462.61	454.8	453.4	442.42	441.12	454.43	458.41	440.56	456.2	446.37
610	451.76	467.13	461.19	439.66	465.28	460	459.28	447.68	448.81	461.29	467.54	447.56	463.97	452.29
612	36.44	38.65	38.55	36.32	38.61	36.2	39.29	37.74	37.16	38.96	39.88	38.12	39.58	37.46
612	36.12	38.94	38.12	36.12	38	36.34	38.24	37.69	36.46	38.48	39.28	37.58	39.26	37.18
BCR	23.88	50.16	6.31	26.82	6.33	1.838	6.25	0.947	6.1	1.197	3.39	0.486	3.22	0.47
Mongol	0.0231	0.284	0.1175	1.464	1.532	1.005	4.9	1.099	8.94	2.086	6.13	0.803	4.81	0.649
C_70b	2.336	1.883	0.474	1.89	0.326	0.846	0.455	0.0643	0.276	0.0181	0.0226	< 0.0031	< 0.020	< 0.0020
C_70c	1.233	1.076	0.341	1.089	0.259	0.181	0.21	0.0289	0.118	0.0049	< 0.0080	0.0053	0.0271	< 0.00158
C_70a	19.86	33.04	3.57	12.56	2.3	2.3	2.35	0.285	1.186	0.1019	0.083	0.0088	< 0.0115	< 0.0027
C_66	323.22	695.97	94.25	385.32	79.95	13.04	53.88	3.41	6.29	0.297	0.243	0.0059	0.048	0.0045
C_69	25.58	823.51	15.44	57.09	15.84	2.82	10.81	1.349	3.78	0.228	0.188	0.0164	0.096	0.0089
A_42	1.016	1.731	0.1858	0.712	0.134	0.0981	0.129	0.0184	0.123	0.028	0.1043	0.0128	0.116	0.0174
A_43	17.44	4.23	2.539	8.44	0.955	0.574	0.767	0.0887	0.516	0.1071	0.259	0.0344	0.168	0.0195
A_44	2.277	2.305	0.438	1.895	0.283	0.915	0.292	0.0413	0.356	0.0671	0.195	0.0347	0.18	0.0174
A_45a	0.899	1.765	0.174	0.669	0.135	0.0825	0.115	0.018	0.1011	0.0244	0.0785	0.0115	0.1094	0.016
A_45b	0.937	1.672	0.1935	0.735	0.123	0.1007	0.0948	0.0191	0.1428	0.0265	0.0873	0.0155	0.0936	0.0167
A_46a	5.73	18.83	1.794	6.8	1.193	0.364	0.723	0.0994	0.555	0.112	0.281	0.035	0.203	0.0291
A_46b	0.905	0.711	0.312	1.068	0.231	0.194	0.23	0.029	0.148	0.035	0.107	0.0094	0.053	< 0.0038
C_CL1	2.44	3.73	0.477	1.93	0.386	1.807	0.761	0.0808	0.529	0.0375	0.075	0.0032	0.0251	< 0.0016
C_CL2	4.18	6.17	0.575	2.17	0.446	1.836	0.367	0.0477	0.153	0.0111	0.0185	< 0.00197	0.015	< 0.00196
C_CL3	62.3	58.26	10.8	39.6	6.23	2.215	5.3	0.523	1.58	0.1187	0.127	< 0.0033	0.05	0.0053
C_CL4	3.46	5.08	0.622	2.09	0.438	1.585	0.369	0.048	0.192	0.0211	< 0.0131	< 0.0028	< 0.0111	< 0.0042
B_1	2.092	3.61	0.347	1.417	0.315	1.057	0.177	0.0421	0.176	0.0138	0.02	0.0069	0.0111	0.0056
B_2	2.7	3.18	0.613	2.57	0.655	1.069	0.406	0.0598	0.275	0.0359	0.052	0.0053	0.032	0.0041
B_12	1.079	1.914	0.216	0.828	0.15	0.1101	0.121	0.0217	0.132	0.0293	0.1114	0.0138	0.1145	0.0224
B_13	2.516	3.57	0.369	1.339	0.308	1.111	0.245	0.0362	0.164	0.0137	-0.0062	0.0117	-0.0118	0.006
B_14	1.163	1.972	0.209	0.85	0.181	0.1041	0.18	0.0223	0.171	0.0396	0.0865	0.0167	0.12	0.0242
B_15	1.098	1.959	0.234	0.873	0.172	0.1011	0.126	0.0242	0.153	0.0288	0.0911	0.0192	0.104	0.0174
610	448.29	464.44	457.42	437.51	462.37	457.39	457.68	447.25	445.82	458.58	466.03	444.14	458.66	449.83
610	445.91	460.55	454.09	437.55	460.68	455.2	455.91	444.9	444.52	456.16	462.07	441.12	455.99	446.08
612	36.38	38.59	38.33	35.88	38.03	36	37.59	37.55	35.91	38.12	39.61	37.43	39.14	36.91
612	36.38	38.54	38.29	35.96	38.19	35.98	38.7	37.48	36.16	38.11	39.36	37.2	38.79	36.71
BCR2G	24.06	50.96	6.47	27.62	6.25	1.908	6.22	0.944	6.05	1.22	3.45	0.462	3	0.477
Mongol	0.0176	0.295	0.1202	1.565	1.83	1.053	5.03	1.14	9.25	2.147	6.25	0.808	4.92	0.621

 Table S4 - LAICPMS rare earth element data for plagioclase

Element	La139	Ce140	Pr141	Nd146	Sm147	Eu153	Gd157	Tb159	Dy163	Ho165	Er166	Tm169	Yb172	Lu175
610	446.52	459.54	454.23	436.24	462.61	454.8	453.4	442.42	441.12	454.43	458.41	440.56	456.2	446.37
610	451.76	467.13	461.19	439.66	465.28	460	459.28	447.68	448.81	461.29	467.54	447.56	463.97	452.29
612	36.44	38.65	38.55	36.32	38.61	36.2	39.29	37.74	37.16	38.96	39.88	38.12	39.58	37.46
612	36.12	38.94	38.12	36.12	38	36.34	38.24	37.69	36.46	38.48	39.28	37.58	39.26	37.18
BCR	23.88	50.16	6.31	26.82	6.33	1.838	6.25	0.947	6.1	1.197	3.39	0.486	3.22	0.47
Mongol	0.0231	0.284	0.1175	1.464	1.532	1.005	4.9	1.099	8.94	2.086	6.13	0.803	4.81	0.649
C_40	0.731	1.598	0.218	0.91	0.212	0.0938	0.187	0.0247	0.044	0.005	0.0066	< 0.0020	< 0.0072	0.0048
C_41	0.234	0.0517	0.0721	0.274	0.039	0.0708	0.144	0.017	0.047	< 0.00157	< 0.0042	< 0.0021	< 0.0107	< 0.0035
C_77	46.64	1.343	13.87	50.75	8.66	1.503	7	0.709	2.38	0.287	0.593	0.0726	0.524	0.0551
C_37	0.0475	0.0728	0.0151	< 0.021	< 0.026	0.0382	< 0.024	< 0.0031	0.0122	< 0.0030	< 0.0122	0.006	< 0.0161	< 0.0020
C_75	0.526	0.127	0.174	0.597	0.117	0.074	0.09	0.0115	0.039	< 0.0040	0.0101	< 0.00171	< 0.0116	< 0.0023
A_19	1.831	0.754	0.399	1.432	0.317	0.627	0.261	0.0407	0.282	0.0498	0.144	0.0207	0.086	0.0185
A_17	0.0763	0.034	0.0163	0.099	0.0173	0.0343	< 0.0127	0.0029	< 0.0127	< 0.0030	< 0.0083	0.0039	< 0.022	< 0.0036
A_12	0.365	0.1216	0.0552	0.251	0.037	0.0348	0.077	< 0.0026	0.052	0.0194	0.053	0.0047	0.0285	0.0047
A_7	0.0418	0.0571	0.0129	0.021	0.05	0.0366	0.084	0.0063	0.035	0.008	0.0305	0.0056	< 0.0163	< 0.0038
A_8	2.489	1.953	0.484	2.16	0.555	0.174	0.599	0.0939	0.631	0.1254	0.412	0.0504	0.41	0.0575
A_13	3.57	2.26	0.738	3.09	0.746	0.265	0.912	0.1561	1.078	0.263	0.668	0.0888	0.456	0.0487
B_1b	0.817	1.388	0.157	0.653	0.041	0.062	0.107	0.0081	0.158	0.0208	0.071	0.0035	0.123	0.0154
B_1	0.699	-0.048	0.0831	0.261	0.048	0.0627	0.047	0.0302	0.239	0.0475	0.166	0.0261	0.109	0.0222
B_2	0.822	1.367	0.142	0.516	0.156	0.0685	0.115	0.013	0.253	0.0445	0.173	0.019	0.179	0.0168
B_6	-0.025	1.037	-0.012	-0.065	-0.026	0.066	0.082	0.0111	0.095	0.0079	0.078	0.0145	0.101	0.017
B_8	1.14	36.6	0.631	2.3	0.512	0.15	0.4	0.0344	0.191	0.0099	0.0212	-0.0043	-0.0172	0.0024
610	448.29	464.44	457.42	437.51	462.37	457.39	457.68	447.25	445.82	458.58	466.03	444.14	458.66	449.83
610	445.91	460.55	454.09	437.55	460.68	455.2	455.91	444.9	444.52	456.16	462.07	441.12	455.99	446.08
612	36.38	38.59	38.33	35.88	38.03	36	37.59	37.55	35.91	38.12	39.61	37.43	39.14	36.91
612	36.38	38.54	38.29	35.96	38.19	35.98	38.7	37.48	36.16	38.11	39.36	37.2	38.79	36.71
BCR2G	24.06	50.96	6.47	27.62	6.25	1.908	6.22	0.944	6.05	1.22	3.45	0.462	3	0.477
Mongol	0.0176	0.295	0.1202	1.565	1.83	1.053	5.03	1.14	9.25	2.147	6.25	0.808	4.92	0.621

 Table S5 - LAICPMS rare earth element data for biotite

Element	La139	Ce140	Pr141	Nd146	Sm147	Eu153	Gd157	Tb159	Dy163	Ho165	Er166	Tm169	Yb172	Lu175
610	446.52	459.54	454.23	436.24	462.61	454.8	453.4	442.42	441.12	454.43	458.41	440.56	456.2	446.37
610	451.76	467.13	461.19	439.66	465.28	460	459.28	447.68	448.81	461.29	467.54	447.56	463.97	452.29
612	36.44	38.65	38.55	36.32	38.61	36.2	39.29	37.74	37.16	38.96	39.88	38.12	39.58	37.46
612	36.12	38.94	38.12	36.12	38	36.34	38.24	37.69	36.46	38.48	39.28	37.58	39.26	37.18
BCR	23.88	50.16	6.31	26.82	6.33	1.838	6.25	0.947	6.1	1.197	3.39	0.486	3.22	0.47
Mongol	0.0231	0.284	0.1175	1.464	1.532	1.005	4.9	1.099	8.94	2.086	6.13	0.803	4.81	0.649
C_84C	< 0.0032	< 0.0015	< 0.0039	0.049	0.503	0.318	6.9	4.3	53.02	12	31.03	3.94	23.67	2.99
C_83_Gt	0.0124	0.0542	0.0087	0.081	0.38	0.254	4.49	3.11	48.89	15.08	49.74	6.82	42.13	5.92
C_83_Gt	0.0036	< 0.0044	< 0.0028	0.057	0.46	0.357	7.5	4.17	49.9	11.08	30.79	4.23	28.05	3.65
C_77_Gt	< 0.0025	< 0.0038	< 0.0021	0.032	0.391	0.371	6.67	4.25	56.77	14.33	42.24	5.64	36.15	4.89
C_80_Gt	0.0246	0.75	0.019	0.107	0.417	0.267	6.38	3.88	50.93	12.66	37	4.97	30.71	4.24
B_1b_Gt	0.0133	-0.0049	0.0043	0.024	0.293	0.267	3.59	2.49	40.61	11.34	30.52	3.18	15.34	1.769
B_2b_Gt	0.0062	0.002	-0.0026	0.079	0.415	0.363	5.13	3.22	48.67	12.44	31.6	3.42	16.86	1.872
B_1_Gt	-0.0041	-0.0034	-0.0037	0.088	0.328	0.275	4.4	2.59	42.07	11.4	29.85	3.16	15.59	1.705
B_2_Gt	0.0073	-0.0046	-0.0042	0.074	0.434	0.336	4.3	2.74	43.37	11.12	28.37	2.97	15.8	1.685
B_3_Gt	-0.0029	0.0036	0.004	0.096	0.314	0.295	4.66	3.08	50.78	14.72	37.51	3.7	17.19	1.912
610	448.29	464.44	457.42	437.51	462.37	457.39	457.68	447.25	445.82	458.58	466.03	444.14	458.66	449.83
610	445.91	460.55	454.09	437.55	460.68	455.2	455.91	444.9	444.52	456.16	462.07	441.12	455.99	446.08
612	36.38	38.59	38.33	35.88	38.03	36	37.59	37.55	35.91	38.12	39.61	37.43	39.14	36.91
612	36.38	38.54	38.29	35.96	38.19	35.98	38.7	37.48	36.16	38.11	39.36	37.2	38.79	36.71
BCR2G	24.06	50.96	6.47	27.62	6.25	1.908	6.22	0.944	6.05	1.22	3.45	0.462	3	0.477
Mongol	0.0176	0.295	0.1202	1.565	1.83	1.053	5.03	1.14	9.25	2.147	6.25	0.808	4.92	0.621

 Table S6 - LAICPMS rare earth element data for garnet